
Article:
Ali, M, Mahmud, T, Heggs, PJ et al. (1 more author) (2020) Zonal modelling of a counter-current spray drying tower. Chemical Engineering Research and Design, 155. pp. 180-199. ISSN 0263-8762

https://doi.org/10.1016/j.cherd.2019.12.018

Zonal Modelling of a Counter-Current Spray Drying Tower

Muzammil Ali, Tariq Mahmud+, Peter John Heggs and Mojtaba Ghadiri

School of Chemical and Process Engineering, The University of Leeds, Leeds LS2 9JT, UK

Keywords: spray drying, counter-current spray tower, zonal modelling, heat and mass transfer
+ Corresponding author; email: t.mahmud@leeds.ac.uk; Tel: +44 113 34 32431

Abstract

A generic multi-zonal modelling methodology for spray drying towers is proposed to provide relatively quick (seconds) simulations on desktop computers for decision making on changing process parameters for automatic process control. A multi-zonal model comprises combinations of all or some of six differing zones: plug-flow, semi-plug-flow and well-mixed zones in either co- or counter-current flow. This approach is demonstrated by predicting the dried powder characteristics of a detergent powder from a pilot-scale counter-current spray drying tower. The types, sizes and locations of the different zones are obtained by a detailed analysis of predictions from a previous 3-dimensional Computational Fluid Dynamics (CFD) simulation of gas and particle flow dynamics and drying kinetics within the tower. The multi-zonal model consists of seven zones – five in counter-current and two in co-current flow. The trends of the predicted gas temperature profiles are close to those from the CFD results. The particle exit temperature, moisture content and residence times over the full particle size distribution (PSD) range are very close to the CFD values unlike the previous simulated results from our plug-flow model. The outcome clearly demonstrates that the prerequisite to have a sound conceptual model of spray drying towers, such as the multi-zonal model developed here, is a detailed knowledge of the gas and particle flow fields within the tower.

1 Introduction

Spray drying is a simultaneous heat and mass transfer operation which is commonly used in industries to remove a liquid phase from a solution or slurry suspension by evaporation. It is carried out co-currently or counter-currently with the drying gas flow. The latter is commonly accompanied by a strong swirling gas flow to increase heat and mass transfer, as a result of which sprayed droplets may coalesce on atomisation and the partially dried particles may agglomerate

and impinge and stick to the walls and then dislodge once fully dried (Francia *et al.*, 2015). The drying particles have usually a wide size distribution and their residence time varies with the particle size (Ali *et al.*, 2017). Due to their interaction with the counter-current swirling gas flow they are concentrated near the wall, moving as a rapid shearing band and interacting with each other and with the wall (Ali *et al.*, 2017). Therefore a predictive analysis of particle drying and the associated gas and solids flows in the tower poses a great challenge.

Various approaches have been used for the modelling of spray drying processes utilizing simplifying assumptions to make a workable model. These can be categorized in terms of the representation of the geometry and of the flows within the tower as being three-dimensional, two-dimensional, one-dimensional (plug-flow) and zero-dimensional (equivalent to a continuous stirred tank reactor (CSTR)) models. The most complete representation of the physics occurring within a spray drying tower is a three-dimensional model using computational fluid dynamics (CFD) software coupled with a drying kinetic model for various cuts of the PSD. This type of model considers the complex three-dimensional gas and droplets/particle flows inside the tower (the gas and the discrete phase velocities vary in the axial, radial and the tangential coordinates), and provides the trajectories of the discrete phase, residence times and accommodates the heat, mass and momentum transfer between phases. Furthermore, the complex particle-particle/particle-wall interactions including coalescence, agglomeration, deposition on the wall and re-entrainment of deposited material back into the gas flow can also be considered. This requires coupling between a population balance model with the multiphase CFD and DEM. This development is very difficult and time consuming, because of the tower size. Also it is imperative that mesh independence is proven, a good numerical accuracy is achieved and that appropriate turbulence models have been used. It is also very necessary to validate the model against experimental measurements. Finally the run times per simulation and computer hardware requirements can be very restrictive. Three-dimensional CFD simulations of spray towers for the drying of various materials, such as detergent, milk, maltodextrin, have been carried out by various researches including Livesley *et al.* (1992), Harvie *et al.* (2002), Huang *et al.* (2004, 2006), Mezhericher *et al.* (2010, 2012), Anandharamakrishnan *et al.* (2010), Wawrzyniak *et al.* (2012) and Ali *et al.* (2017).

In the two-dimensional CFD models, the gas and discrete phases are allowed to vary in the axial and radial coordinates only, because angular symmetry around the vertical axis of the tower is assumed. These models still need to be checked for the above mentioned factors, but the computer run times and memory will be much shorter than those for the three-dimensional simulations. However for counter-current spray towers, these two-dimensional representations cannot accommodate the swirling gas flows and hence cannot reproduce realistic

droplets/particles trajectories. A number of researchers including Crowe (1983), Livesley *et al.* (1992), Oakley and Bahu (1993), Langrish and Zbicinski (1994), Zbicinski (1995), Kieviet (1997), Kieviet and Kerkhof (1997), Southwell *et al.* (1999), Straatsma *et al.* (1999), Zbicinski and Zietara (2004), Huang and Mujumdar (2006) and Mezhericher *et al.* (2008, 2010) have carried out simulations of spray drying of various materials, such as milk, maltodextrin, detergent, using this approach.

One-dimensional models do not need the use of CFD for analysis and both the gas and discrete phases (droplets/particles) are considered to be in plug-flow along the height: the so called plug-flow model. The models are a set of coupled non-linear ordinary differential equations for mass and energy balances coupled with a single particle drying model and accommodate the different size cuts of the PSD. The model for co-current flow towers is an initial value problem, but the model for the countercurrent towers is a boundary value problem. The numerical solution methodology is different for the two different flows, and it is imperative that convergence, stability and compatibility have been demonstrated for the numerical simulations. These can be easily run on a desktop PC and the run times are only orders of seconds compared to hours for the two-dimensional and days for the three-dimensional models, respectively. These relatively simple models reveal useful information about operating parameters (such as temperature, moisture content, mass flow etc.) of the discrete and gas phases along the height of the tower. They can be used to carry out more extensive investigations of the spray drying process operation, including the determination of spray nozzle height, and solution/slurry flows from the spray nozzles (in case of multiple nozzles at different heights) to predict the influence of operating conditions on the dried powder characteristics. The qualitative nature of the outcomes of these investigations provides an excellent starting point for the more time consuming quantitative CFD simulations. Various researchers including Parti and Palancz (1974), Gauvin *et al.* (1975), Katta and Gauvin (1975), Keey and Pham (1976), Topar (1980), Montazer-Rahmati and Ghafele-Bashi (2007), Ali *et al.* (2014) and Pinto *et al.* (2014) have applied this approach for the prediction of the spray drying of various materials in the food, pharmaceutical and chemical industries within both co-current and counter-current towers.

Finally, zero-dimensional models are the very simplest spray drying models and are equivalent to a continuous stirred tank reactor (CSTR) system. The simulations are based on the overall mass and energy balances between the drying gas and the droplets/particles at the inlet and outlet of the tower, and do not require or provide any information about the dryer design parameters, e.g. tower height and diameter, and spray nozzle position. These models are only as good as the experimental measurements taken at the inlets and exits of pilot plant and industrial towers, but

are also essential for checking the overall accuracy of the heat and mass balances of the more sophisticated models discussed previously.

The characterisation of zones within a counter-current spray dryer has been carried out experimentally by Ade-John and Jeffreys (1978) based on the air flow and droplets residence times in a transparent spray dryer. The influence of operating conditions on the volumes of different zones was also studied, thus providing a potential for zonal modelling of these spray dryers.

A reliable and representative modelling approach, which will provide reasonable predictions of the complex interaction of the gas and the discrete phases at different heights, is required for the search of optimized process parameters. Such a model should have short run times and be run on a PC by the plant operators and allow for automatic process control. A simplified multi-zonal modelling approach is therefore proposed in this study by interconnected zones comprising CSTR, plug-flow and semi-plug-flow models. The latter is a combination of CSTR and plug-flow models. The types, dimensions and locations of the zones are identified from the predictions of detailed three-dimensional CFD modelling investigations. This proposed approach is illustrated by the investigation of the counter-current spray drying of detergent powders in an industrial pilot-scale tower. A three dimensional CFD simulation coupled with the semi-empirical single slurry droplet drying model of Hecht (2012) for the drying kinetics of the individual cuts of the PSD carried out by Ali *et al.* (2017) provides the information required to generate the various zones in the tower. Furthermore, the results from this multi-zonal approach, the original CFD simulations and the predictions from a plug-flow of the same tower (Ali *et al.*, 2014) with identical processing conditions are presented and discussed.

2. A Generic Approach to Multi-Zonal Modelling

In the multi-zonal modelling approach, a spray drying tower is divided into a number of interconnected compartments (zones), each of which can be a CSTR, a plug-flow or a semi-plug-flow representation and with the two phases either in counter- or co-current flow. Figures 1 (a), (b) and (c) represent zones in counter-current flow for CSTR, plug-flow and semi-plug-flow models, respectively. Figures 1 (d), (e) and (f) are the three models in upward co-current flow respectively. These latter three figures can be easily inverted for downward co-current flow.

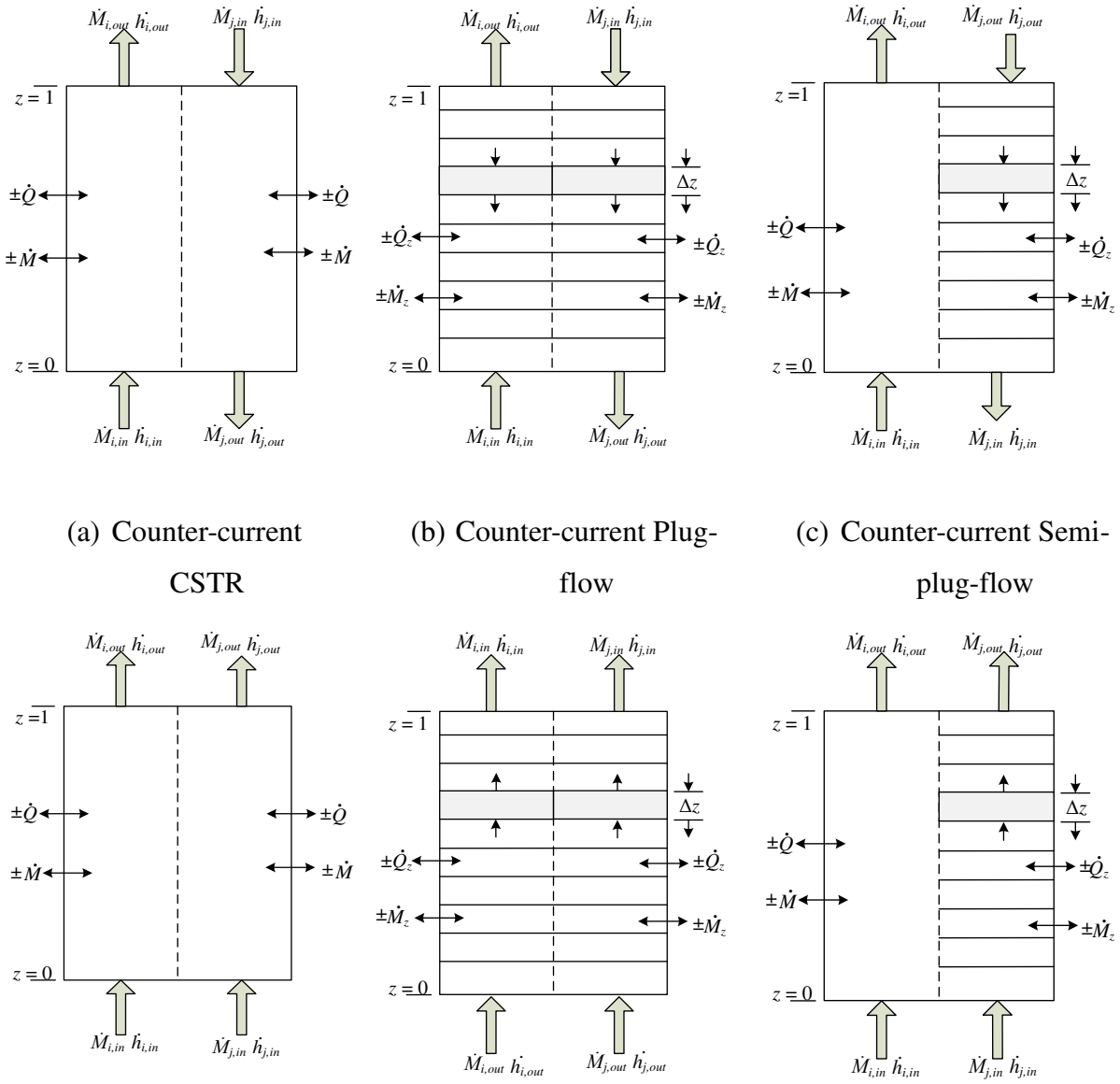

(a) Counter-current CSTR

(b) Counter-current Plug-flow

(c) Counter-current Semi-plug-flow

(d) Co-current CSTR

(e) Co-current Plug-flow

(f) Co-current Semi- plug-flow

Figure 1: Schematic diagrams of possible types of zones: CSTR, Plug-flow and Semi-plug-flow.

Within each type of zone, the mass, heat and momentum transfer between the phases must be accommodated: hence the vertical dotted line. The interiors of the schematic diagrams for the CSTR zones 1(a) and 1(d) are left blank to imply that the zone is a fully mixed model and the outlet parameters from the zone will be obtained from a set of algebraic equations. For the plug-flow zones 1(b) and 1(e) the interior of the zone is divided into slices to indicate that the parameters of the phases within and at the exit of the zone are position dependent and their values will be obtained from the numerical solution of a set of coupled ordinary differential equations. These representations will either be a boundary value problem for the counter-current flow Figure 1(b) or an initial value problem for the co-current flow Figure 1(e). For the semi-plug-flow zones,

Figures 1(c) and 1(f), the interiors are a combination of the CSTR and plug-flow representations for either phase.

Only the average mass and enthalpy flows of both phases are allowed to cross the upper and lower interfaces of a zone, and only enthalpy and/or mass of the gas, either total or distributed, may traverse the vertical interfaces of a zone. No variation in the radial direction within a zone is allowed, but several zones across a radial part of the tower can be specified. The data required at the upper or lower interfaces (z = 0 and/or z = 1) of any type of zone for the continuous gas phase are as follows:

$$\dot{M}_g, T_{sat}, \text{composition and physical properties} \tag{1}$$

and for each cut of the discrete phase are

$$M_p, T_p, u_p, w_l, d_p, n \text{ and physical properties} \tag{2}$$

The values of the parameters detailed in equations (1) and (2) are obtained from the feed conditions to the tower and from the results of a three-dimensional CFD simulation of the gas and solids flows in a tower once the number, dimensions, positions and type of zones have been specified. The enthalpy transfer, either total ($\dot{Q}$) or distributed ($\dot{Q}_z$), and gas mass flow across the vertical interfaces of the zones will also be obtained from the CFD simulation. For a zone positioned at the outer radius of the tower, there will be no mass flow and the enthalpy transfer will be heat loss from the tower wall.

The combination of different zone representations and the directions of the flow of the phases within them will depend upon the flows in the tower, i.e. counter- or co-current, and within regions where differing physical/chemical phenomena occur. It is anticipated that a tower operating with the two phases in co-current flow, then all the zones will be in co-current flow, but this cannot be specified *a priori,* because recirculation of gas and solids can occur. For a counter-currently operating tower, it is anticipated that the combination will be a mixture of CSTR, plug-flow or semi-plug-flow zones in counter- and co-current flow depending upon the region within the tower. The combination of the sizes and types of zones need to be specified on the basis of a detailed analysis of predictions obtained by a three-dimensional CFD simulation of the tower. For example, in the regions where the process parameters (such as temperature and moisture concentration) of the gas and dispersed phases (droplets/particles) are fairly uniform, a CSTR model is the most convenient representation, Figures 1(a) and 1(d). On the other hand, in regions where strong gradients of gas properties and droplet/particle concentrations exist, a plug-

flow model is required, Figures 1(b) and 1(e). If one of the phases remains fairly uniform and the other phase exhibits strong gradients, then a semi-plug-flow approach is more appropriate, Figures 1(c) and 1(f). In all these figures, the subscripts *i* and *j* are for either phase. This multi-zonal modelling methodology is generally applicable to any co-current or counter-current spray drying tower.

3. Zonal Modelling of a Counter-Current Spray Tower

The proposed multi-zonal representation is applied to an industrial pilot scale tower used for the counter-current spray drying of detergent powders at the P&G Technical Centres, Newcastle-upon-Tyne, UK. Experimental data from this tower have been analysed by a three dimensional CFD simulation by Ali (2014) and Ali *et al.* (2017). Both references contain the details of the simulation and the predictions are used as the basis for devising a zonal model by dividing the tower into zones and for providing the interfacial process variables. A one dimensional plug-flow model has also been published for the same tower by Ali *et al.* (2014).

A schematic of the tower is given in Figure 3(a). It comprises two sections, a lower conical section and a cylindrical upper section. The dimensions of the radii and height of the tower are not disclosed due to confidentiality reasons, and so, normalised radii ($0 \leq r \leq 1$) and height ($0 \leq z \leq 1$) are used. The central axis of the tower is at $r = 0$ and the outer bound of the flow region is $r = 1$. The conical section lies between $z = 0$ and $z = 0.14$, and the top of the cylindrical portion is at $z = 1$. The slurry feed point is at $r = 0$ and $z = 0.67$, and the hot gas enters at $r = 1$ and $z = 0.14$.

The smallest number of zones would be three: the conical section from the hot gas feed inlet down to the bottom exit, the cylindrical section from above the conical section up to the slurry feed point and finally from the slurry feed point to exit at the top. However due to the complex nature of the mass, heat and momentum transfer between the downward flow of the droplets/particles and upward flow of the gas, some of these three zones will have to be compartmentalized.

The drying gas is a mixture of combustion products from a direct fired furnace using natural gas as the fuel and is mixed with entrained ambient air to provide an inlet gas temperature of 563 K (290°C). However, in the simulations the hot gas is represented as air with a moisture mass fraction of 0.023, which accommodates the humidity and combustion products. This hot gas enters via several downward facing tangential-entry inlets positioned in the upper region of the conical region of the tower at $r = 1$ and $z = 0.14$. These impart considerable swirl to the gas flow,

which initially travels downwards in a spiral flow field and then turns vertically upwards due to the suction at the top of tower where the gas exits. This reversal of the gas flow entrains cold air into the bottom of the conical region.

The slurry at a mass flux of 0.21 kg/m^{2}s and temperature of 358 K (85°C) is atomised using a pressure-swirl hollow-cone nozzle. The droplets flow in the downward direction from a position $r = 0$ and $z = 0.67$ in the cylindrical part of the tower. In the absence of measurement of the initial droplet sizes, the measured size distribution of dried detergent particles collected from the bottom of the spray tower is used as the initial slurry droplet size distribution in the simulation in line with our previous study (Ali *et al.*, 2014). This may be a valid assumption if coalescence and agglomeration occur in the dense spray region very close to the nozzle, and the resulting size distribution thereafter remains fairly constant. The size range of dried particles collected from the tower is from 100 µm to 2300 µm. The particle size distribution measured by gravimetric analysis by sieving using 10 BS sieves is fitted by a Rosin-Rammler distribution (Rosin and Rammler, 1933), given by equation (3) using a size constant (d_m) of 750 µm and distribution parameter (u_s) of 1.35 with an R^2 value of 0.98.

$$Y_d = \exp\left\{-\left(d_p / d_m\right)^{u_s}\right\} \tag{3}$$

In the simulation, 23 discrete sizes were obtained from equation (3) to approximate the droplet size distribution. All droplets exit the nozzle at the same velocity. The influence of number of size cuts on the outlet powder parameters and the size of Δz has been assessed in the same tower by Ali *et al.* (2014). The falling sprayed droplets come in contact with upward flowing hot gas, which results in the removal of moisture and hence the drying of the droplets/particles. However some fine particles: all particles of size 100 µm and smaller, and a fraction of the 200 µm size, get entrained by the gas and leave from the top of the tower based on CFD results (Ali *et al.,* 2017). The 100 µm and smaller size particles comprise 75% of the total mass of the entrained particles. All particle sizes > 200 µm and a fraction of 200 µm sizes exit from the bottom of the tower.

The single droplet drying model of Hecht (2012) is used here in the zonal representations and previously was used in the CFD and the one-dimensional plug-flow simulations of the tower. For completeness, it is included in Appendix A of this discourse.

The inlet operating conditions, the dimensions of tower wall and insulation are listed in Table 1 and these are identical to those used for the previous simulations. Also listed in Table 1 are the

thermodynamic and physical properties used in the drying model. The detergent slurry composition cannot be disclosed. However, the composition is very similar to the detergent slurry studied by Griffith *et al.* (2008), which consists of 28% moisture along with other major components, including surfactant, binder and polymer.

Table 1: Model input specifications.

Operating Inlet Conditions	
Slurry mass flux, kg/m^{2}s	0.21
Slurry inlet temperature, K	358
Hot gas mass flux, kg/m^{2}s	0.92
Hot gas temperature, K	563
Entrained air mass flux, kg/m^{2}s	0.046
Ambient temperature, K	293
Tower Wall	
Wall metal thickness, m	0.006
Metal thermal conductivity, W/m K	18.8
Insulation thickness, m	0.105
Insulation conductivity, W/m K	0.04
Deposit layer thickness, m	0.03
Deposit material conductivity, W/m K	1.3
Thermophysical properties	
Specific heat of dried particle, J/kg K	1500
Specific heat of solvent, J/kg K	4180
Specific heat of vapour, J/kg K	1900
Density of slurry, kg/m^3	1200
Latent heat of vapourisation, J/kg	2.26×10^6
Moisture diffusivity, m^2/s	3.0×10^{-11}
Vapour diffusivity, m^2/s	2.6×10^{-5}

3.1 CFD Simulation Results

Predicted representative droplet/particle trajectories and the corresponding gas temperature and moisture mass fraction profiles in the tower, reported by Ali *et al.* (2017), are summarized to lay the foundations for partitioning of the tower into zones. Above the spray nozzle, all the droplets/particles of sizes of 100 μm and smaller, and a portion of 200 μm particles are dispersed

fairly uniformly, and are entrained by the gas and carried upwards. The rest of the 200 μm sized and larger droplets/particles (≥ 200 μm) travel downwards in a hollow-cone pattern until they collide with the wall. Some rebound and move in a downward spiraling motion in the near-wall region flow, whilst others adhere to the wall and eventually get sheared off due to the swirling particle/droplet laden gas. This continues as the particles enter the bottom conical section, and finally, exit from the bottom of the tower.

The gas temperature in the tower is relatively uniform at around 380 K (107°C) in the section above the spray region and the top of the tower. This low gas temperature exists near the spray region due to rapid evaporation of the droplets at 358 K (85°C), which causes rapid cooling of the gas. Below the spray region, the gas temperature close to the wall in the cylindrical region of the tower is around 40 K smaller compared to that in the core region. Eventually, the gas temperature increase extends to the central region of the tower due to the swirling motion of the gas emanating from the cone region. The hot gas at 563 K (290°C) enters by several nozzles and a downward swirling flow develops. There is a region close the gas injection nozzles where the gas remains at the inlet temperature, but the temperature then falls in a three dimensional spatial pattern due to the cyclonic flow of the gas: the majority of the gas is dragged downwards by the spirally falling particles close to the wall, but a hot portion goes up close to the wall into the cylindrical section of the tower. However the temperature of the swirling gas closer to the central region begins to fall due to mixing with a central core of upward flowing cooler gas. This upward flow of gas contains cold air at 293 K (20°C) sucked in from the base of the tower, which progressively mixes with the spirally flowing hot gas. Eventually this central core of gas travels upward into the core of the cylindrical section of the tower, but at a temperature approximately 55 to 60°C cooler than the hot gas injected into the tower.

The gas moisture fraction profile in the tower can be split into three regions: above the spray nozzle it is almost uniform at 0.081 w/w, below the nozzle in the core of the spray region it is higher at 0.102 w/w due to the moisture in the slurry, and then below the spray region, it is the lowest at around 0.05 w/w. The cold air entrained through the tower base has a moisture content of 0.01 w/w and the inlet hot gas contains 0.023 w/w.

In addition the CFD results have been further analysed with respect to the tangential gas velocities at various heights in the tower.

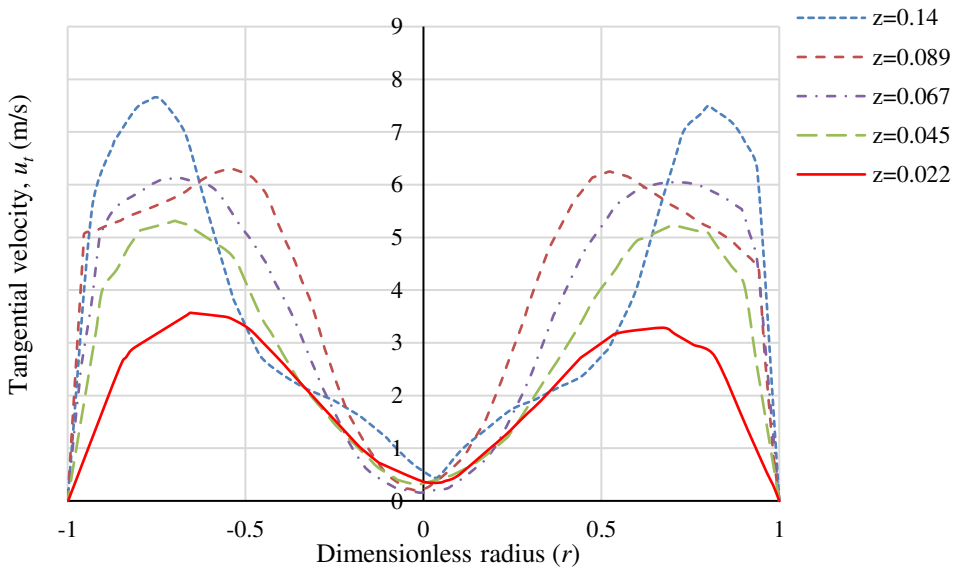

(a)

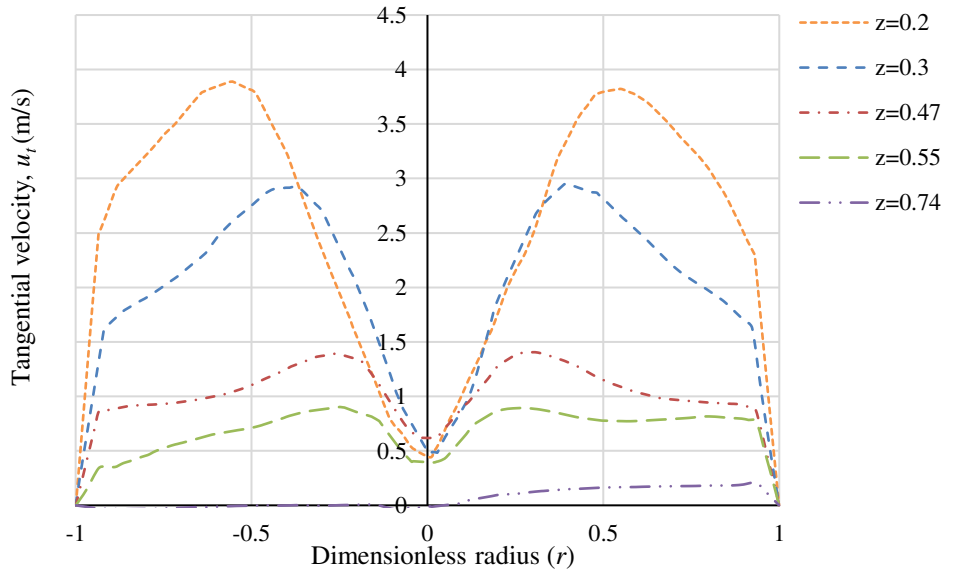

(b)

Figure 2: Plots of the radial profiles of tangential gas velocity at seven heights within the (a) conical and (b) cylindrical sections of the tower.

Figure 2(a) is a plot of the tangential gas velocity profiles in the conical section of the tower from the hot gas inlet at $z = 0.14$ down to close to the bottom exit at $z = 0.022$. These profiles represent a very strong vortex motion occurring at the hot gas inlet and the strength of the vortex progressively diminishes down to $z = 0.022$. The tangential flow in the conical section appears to be a combination of free vortex (near the wall) and forced vortex (in the inner core from roughly 0.75 dimensionless radial position inwards) and this ensures that all the particles move spirally downward close to the contours of the conical section and exit from the bottom of the tower. Likewise in Figure 2(a) there is central core region with very little tangential influence and here the gas is flowing upwards and entraining cold air into the bottom of the tower.

Figure 2(b) is a plot of the tangential gas velocity profiles in the cylindrical part of the tower from just above the conical section at $z = 0.2$ up $z = 0.74$, which is slightly above the slurry input at $z = 0.67$. The vortex motion emanating upwards from the conical section is quickly losing its strength and at $z = 0.55$ it has almost become close to a plug-flow. It is close to this point that the downward swirling motion of the atomised slurry droplets/particles is felt and the droplets/particles have made contact with the cylindrical wall of the tower. The tangential gas velocities are completely absent at $z = 0.74$, which is above the slurry injection point of $z = 0.69$ and there is now plug-flow of the gas.

These gas velocity profiles along with temperature, moisture and residence time profiles of the particles in the tower will be addressed later for each of the zones representing the tower. The above information is used as the basis for the multi-zonal design of the tower as outlined in the next section.

3.2 Zonal Model of the Tower

The tower was initially sub-divided into five zones as depicted schematically in Figure 3 (a), where the final zone 5 for the conical section of the tower was a countercurrent semi-plug-flow configuration, Figure 1(c). However this representation could not handle the severe downward swirl caused by the hot inlet gas nozzles, the subsequent reversal of this flow to an upward direction due to the suction at the top of the tower and the resulting ingress of the cold air through the bottom exit. Therefore the tower has been divided into seven zones: the original zones 1 to 4 and the conical section into a further three zones as illustrated in Figure 3 (b). The position and size of each of these zones have been obtained by scrutinising the gas and droplet/particle flow profiles reported by Ali *et al.* (2017) along with more localised CFD predictions of radial profiles of mass flow, moisture content and temperatures of both gas and particles, and residence times of the various size cuts of the PSD. A further important consideration is the difference between the gas temperature profiles at the centreline and in the near-wall region over the height of the tower. These have been obtained from the CFD predictions and are plotted against the height of the tower in Figure 4.

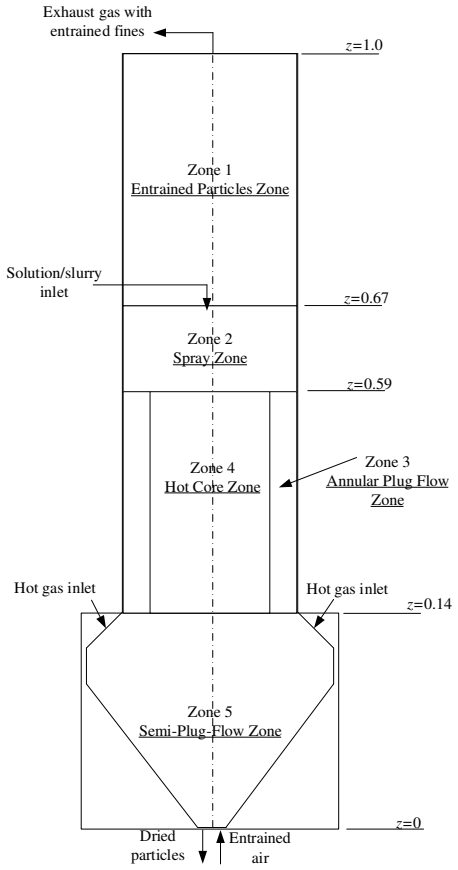

(a)

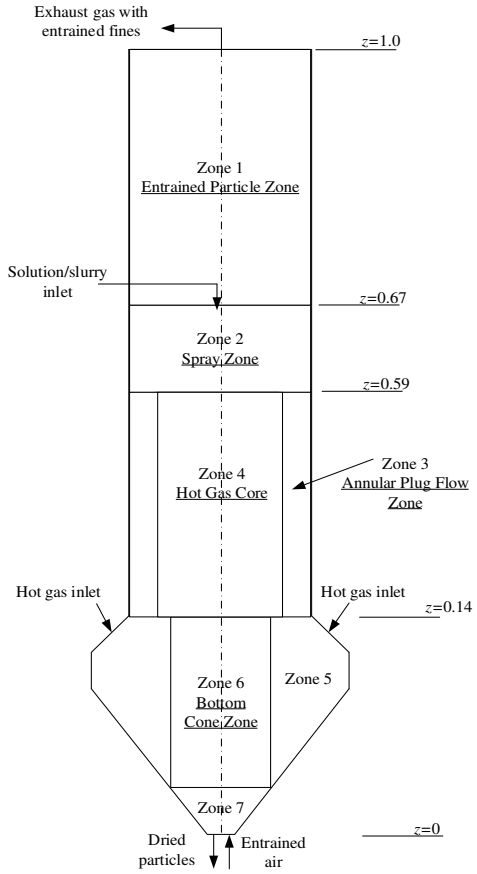

(b)

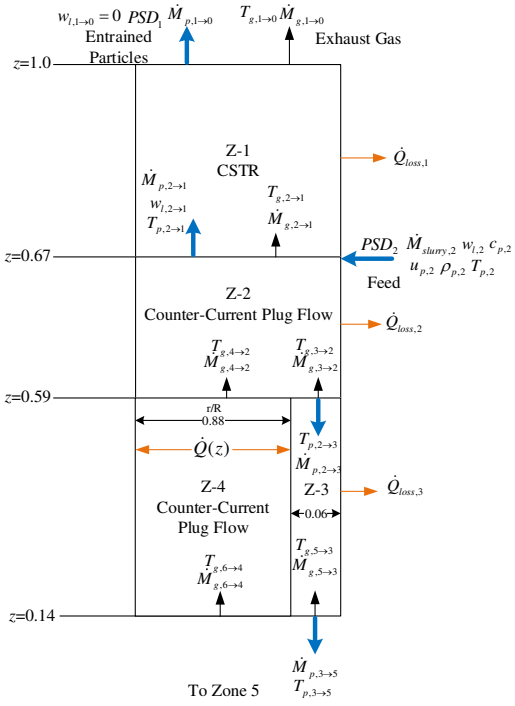

(c)

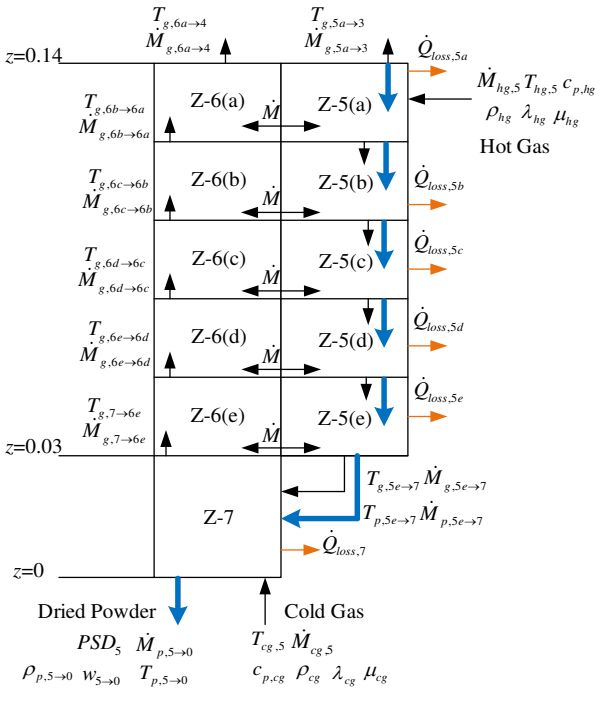

(d)

Figure 3: Schematic diagram of the spray drying tower at P&G Newcastle Technical Centres, UK with (a) the original five zones and (b) the final seven zones representing the tower with (c) connectivity between Zones 1 to 4 and (d) connectivity between Zones 5, 6 and 7.

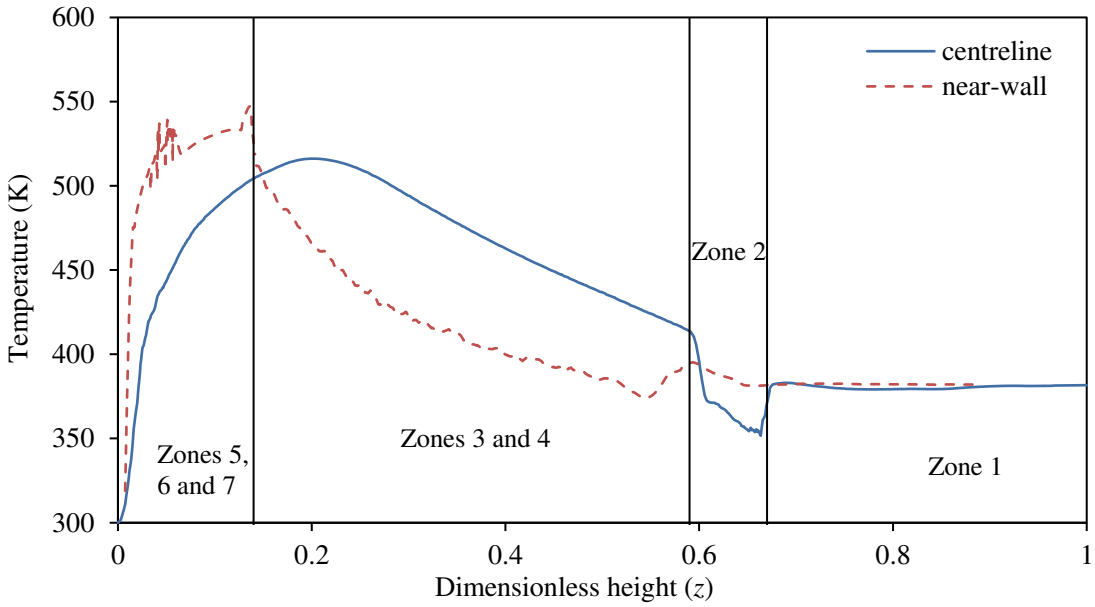

Figure 4: Gas temperatures at the centreline and in the near-wall region of the tower over the dimensionless height.

All the zones are based on the vertical axis of the tower (see Figure 3(b)) and cover the dimensionless radius range of $0 \leq r \leq 1$, due to the assumption of symmetry. The types of zonal configurations and the variables (either specified or evaluated) at the horizontal interfaces of Zones 1 to 4 are detailed in Figure 3(c). Only heat loss crosses the outer vertical interfaces of Zones 1, 2 and 3. Similar details for Zones 5, 6 and 7 are displayed in Figure 3(d). However Zones 5 and 6 are each divided into five equal parts (a) to (e) in order to accommodate the severe swirling caused by the nozzles of the incoming hot gas and the subsequent flow reversal up the column. The vertical interfaces between the adjacent parts of Zones 5 and 6 allow for the exchange of both enthalpy and gas flow. Heat loss occurs from each subsection of Zone 5 and the last Zone 7, where entrained cold air enters and the falling particles exit this last zone.

The connected zones depicted in Figures 3 (c) and (d), and the mathematical representations of each of the zones *in toto* represent a boundary value problem. A numerical solution of the system requires iteration, for which a logic flow diagram of the algorithm is given in Figure S6 in the supplementary material and discussed in Section 3.2.5. However firstly the types of each zone are now described in detail.

3.2.1 Zone 1 (Entrained Particles Zone)

Zone 1 is the entrained particle region and extends from above the spray nozzle to the outlet ($0 \leq r \leq 1$ and $0.67 \leq z \leq 1$). This zone is specified as a co-current CSTR configuration, Figure 1 (d).

The gas and particles both flow upwards in this zone from Zone 2 and exit the zone from the top of the tower. The decision to specify this as a CSTR configuration came about by considering the CFD predicted gas temperature profiles and solids concentration profiles in Figure 5. There is very little difference between gas temperatures at the centreline and the near-wall throughout this Zone 1, as shown in Figure 4. As depicted in Figure 5(a), where four radial temperature profiles are plotted and only at z = 0.67 (just above the spray nozzle) is there any significant variation. The droplets/particles above the spray nozzle are dispersed randomly and this is confirmed by the radial concentration distributions of solids at different heights in Figure 5(b). The gas flow contains entrained droplets/particles of sizes up to 200 µm (Ali *et al.*, 2017).

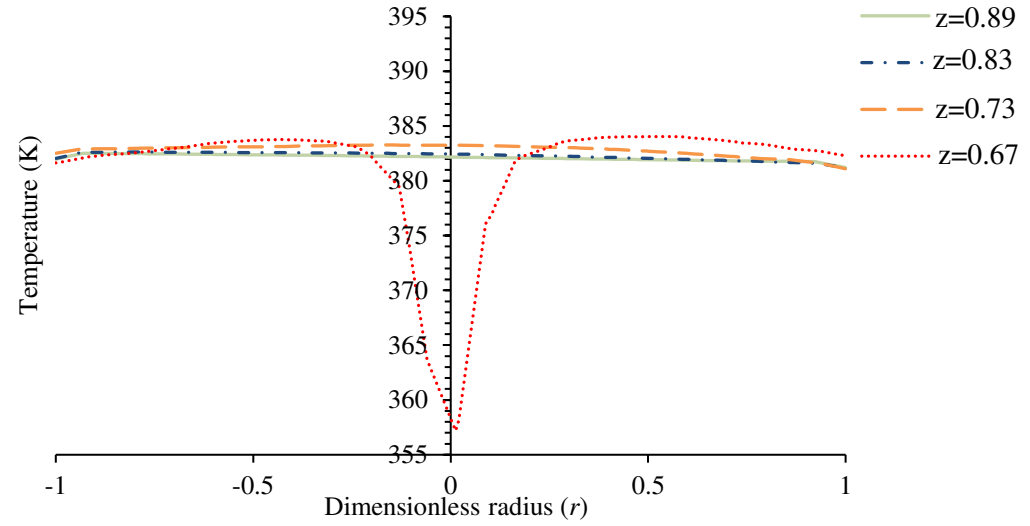

(a)

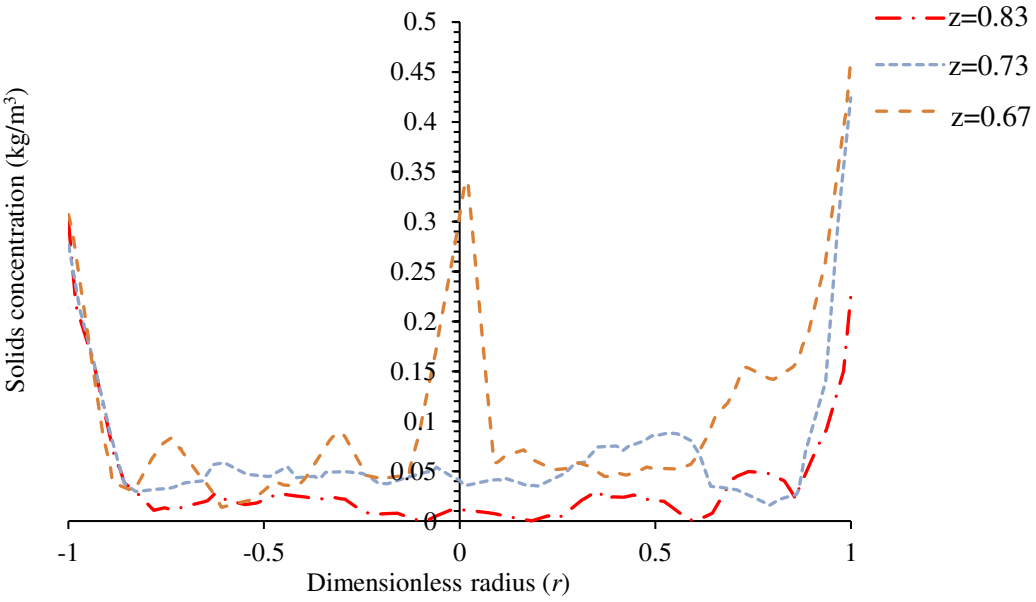

(b)

Figure 5: CFD predicted radial profiles in Zone 1 (a) gas temperature profiles and (b) concentration of solids.

The variables at the horizontal interfaces of Zone 1 are detailed in Figure 3(c), where the subscripts $2 \to 1$ represent the variables entering from Zone 2, and $1 \to 0$ are variables exiting from the top of the tower. The temperatures of the gas and particles throughout this zone are at the values leaving the zone: $T_{g,1\to0}$ and $T_{p,j,1\to0}$ respectively. The heat and mass transfer between the gas phase and the droplets/particles and the heat losses from this zone are modelled by the following overall energy balance:

$$\underbrace{T_{g,2\to1}\dot{M}_{g,2\to1}c_{p,g,2\to1}}_{\text{Enthalpy of gas entering Zone 1}} + \underbrace{\sum_{j=1}^{J} T_{p,j,2\to1}M_{p,j,2\to1}n_j\left[\left(1-w_{l,j,2\to1}\right)c_p + w_{l,j,2\to1}c_{p,l}\right]}_{\text{Total enthalpy of droplets/particles entering Zone 1}}$$

$$= \underbrace{\dot{M}_{g,1\to0}c_{p,g,1\to0}T_{g,1\to0}}_{\text{Enthalpy of gas leaving the Zone 1}} + \underbrace{\sum_{j=1}^{J} T_{p,j,1\to0}M_{p,j,1\to0}n_j\left[\left(1-w_{l,j,1\to0}\right)c_p + w_{l,j,1\to0}c_{p,l}\right]}_{\text{Total enthapy of particles leaving Zone 1}} \quad (4)$$

$$+ \underbrace{(\dot{M}_{g,1\to0} - \dot{M}_{g,2\to1})h_{fg}}_{\text{Enthalpy of evaporation}} + \underbrace{2\pi\, r_i H_{1,} U_1 (T_{g,1\to0} - T_{amb})}_{\text{Heat loss from Zone 1}}$$

The specific heat of the gas entering and leaving the zone is given by equations (5) and (6) respectively:

$$c_{p,g,2\to1} = (1-w_{g,2\to1})c_{p,air} + w_{g,2\to1}c_{p,vap} \quad (5)$$

$$c_{p,g,1\to0} = (1-w_{g,1\to0})c_{p,air} + w_{g,1\to0}c_{p,vap} \quad (6)$$

3.2.2 Zone 2 (Spray Zone)

Zone 2 ($0 \le r \le 1$ and $0.59 \le z \le 0.67$) is represented by a counter-current plug configuration, Figure 1(b). The height of this zone is taken from the location of the spray nozzle (z = 0.67) to the location where the droplets impinge on the wall (z = 0.59). In Figure 4, the centreline temperature falls significantly due to rapid cooling caused by the drying of the droplets. The smaller sizes in the PSD are almost completely dried in this zone and get entrained into the gas flow and go upwards into Zone 1. The near-wall temperature also falls, but much less. The slurry at 358 K (85ºC) and about 60 – 75 bar is atomised into droplets using a hollow-cone pressure nozzle. The spray cone angle is taken to be 40° based on data provided by the vendor.

The CFD predicted gas temperature and mass flow profiles across the radius of the tower at different heights in this zone are depicted in Figure 6. A complex radial variation of gas temperature exists as depicted in Figure 6(a). Just below the spray nozzle (z = 0.67 - 0.65 and r = 0), the rapid evaporation of moisture from the droplets causes a dramatic cooling of the gas. This drop in the centreline temperature becomes less below the nozzle (z = 0.63 - 0.61), and at z

= 0.59, the gas temperature is higher in the central region and then falls approaching the wall. This is the reason why the centreline and near-wall temperature profiles in Figure 4 change dramatically in the region in Zone 2.

Figure 6(b) is a plot of the normalised mass flow of the gas (based on inlet gas mass flow) in this spray zone. In the central region from $z = 0.65$ down to 0.61, the flow is in the downward direction (negative), because the gas flow is entrained by the downward momentum of the droplets in the spray, whereas closer to the wall, the flow is positive and moving counter-current to the droplets. At z = 0.59, the flow profile across the radius is positive except at the wall and the centreline, because the gas is no longer entrained by the spray.

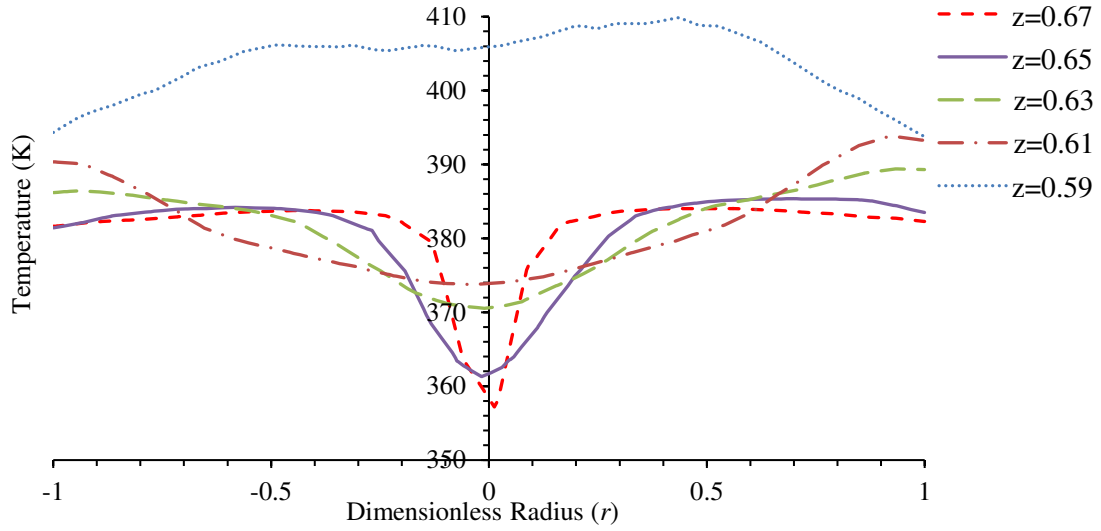

(a)

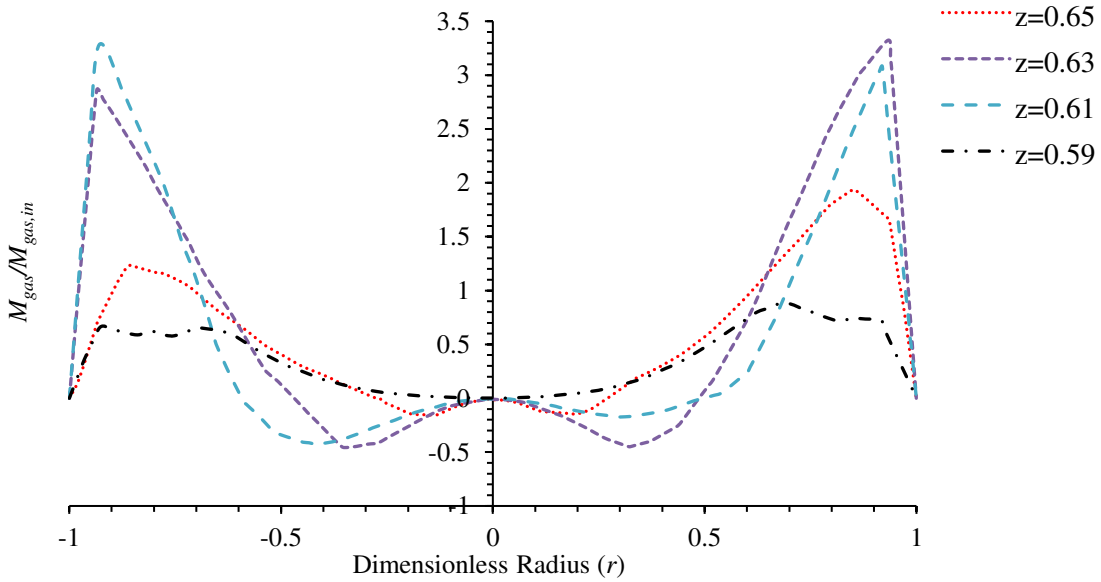

(b)

Figure 6: CFD predicted gas profiles across the radius of the tower at four heights in Zone 2 (a) gas temperature and (b) gas mass flow.

Modelling this relatively short zone by the range of types of zones depicted in Figure 1 is challenging due to the highly non-uniform gas flow and temperature distributions, and the presence of the spray of droplets. However, Ali *et al*. (2014) provides credence in specifying a counter-current plug-flow configuration based on the earlier experience of simulating the entire tower by a plug-flow representation. Feed droplets entering this zone are assumed to be well dispersed over the entire cross-sectional area of the zone at z = 0.67. They flow downwards against the upward flowing combined hot gas streams leaving Zones 3 and 4. The smaller droplets/particles (up to 200 μm diameters) in this zone get entrained by the gas flow: particles of size 100 μm size and smaller comprise 75% of the total mass of the particles entrained and exit into Zone 1 with the gas. The remaining fraction of 200 μm and larger sized particles flow downwards and enter Zone 3.

The temperature profile of the gas phase is calculated using the following equation:

$$\underbrace{\dot{M}_{g,2} c_{p,g,2} \frac{\mathrm{d}T_{g,2}}{\mathrm{d}z}}_{\substack{\text{Heat transfer from} \\ \text{the air to the droplets}}} = \underbrace{\sum_{j=1}^{\mathrm{J}} \alpha_j A_{p_j} (T_{p_j,2} - T_{g,2}) \cdot \frac{n_j}{\tilde{u}_{p,j}}}_{\substack{\text{Total heat input to the} \\ \text{droplets by convection}}} + \underbrace{\sum_{j=1}^{\mathrm{J}} \left(\frac{\mathrm{d}M_l}{\mathrm{d}t} \right)_j c_{p,vap} (T_{p_j,2} - T_{g,2}) \cdot \frac{n_j}{\tilde{u}_{p,j}}}_{\text{Sensible heat to the evaporated vapours}} + \underbrace{2\pi r_i U (T_{amb} - T_{g,2})}_{\text{Heat loss to the environment}} \tag{7}$$

The mass rate of the gas changes due to the evaporation of moisture from the droplets and is evaluated using the following equation:

$$\frac{\mathrm{d}\dot{M}_{g,2}}{\mathrm{d}z} = \sum_{j=1}^{\mathrm{J}} \frac{-n_j}{\tilde{u}_{p,j}} \left(\frac{\mathrm{d}M_l}{\mathrm{d}t} \right)_j \tag{8}$$

The gas specific heat varies along the height due to addition of water vapour and has a similar form as given by equations (5) and (6). The weight fraction of water vapour in the gas is obtained from a mass balance on the gas flow at any height z as follows:

$$\dot{M}_{g,2} \left(1 - w_{g,2}\right) = \dot{M}_{hg,5(a)} + \dot{M}_{cg,7} \tag{9}$$

where $\dot{M}_{hg,5(a)}$ is the mass flow of hot gas entering the tower at Zone 5(a) and $\dot{M}_{cg,7}$ is the flow of entrained cold air into Zone 7 at the bottom of the tower.

The temperature profile of the droplets/particles for each cut of the PSD is calculated using the following equation:

$$\underbrace{M_{p,2}c_{p,drop}\tilde{u}_p\frac{\mathrm{d}T_{p,2}}{\mathrm{d}z}}_{\text{Heat absorbed by the droplet/particle}}=\underbrace{\alpha_p A_p(T_{g,2}-T_{p,2})}_{\text{Heat input to the droplet/particle by convection}}+\underbrace{h_{fg}\frac{\mathrm{d}M_l}{\mathrm{d}t}}_{\text{Heat consumed in vapourizing the moisture}} \tag{10}$$

The heat transfer coefficient of the droplet/particle, α_p in equation (10) is calculated from the Ranz and Marshall (1952) correlation. The drying rate of the droplets/particles is calculated using the semi-empirical droplet drying model of Hecht (2012) and is detailed in the Appendix A, using equations (A.4), (A.18) and (A.19), representing the drying rates at different stages. The droplet/particle velocity is calculated by solving the equation of motion for the particles equation (A.24) in the Appendix A. Once particles entrained by the gas flow within the zone reach their terminal velocity, calculation of that particle size is stopped and the velocity is maintained at this value. Also the minimum velocity of particles exiting the zone is limited to their terminal velocity.

The initial velocity of the droplets ($u_{p,o}$) is considered to be constant for all sizes and is calculated using equation (11a).

$$u_{p,o}=\frac{\dot{M}_{slurry}}{\rho_{slurry}\pi\left(r_o^2-r_c^2\right)\cos\left(\frac{\theta}{2}\right)} \tag{11a}$$

The above equation requires the radius of the air core (r_c) and spray cone injection angle (θ). The injection angle is taken to be 40° based on vendor provided data and the radius of the air core is taken from the data reported by Nelson and Stevens (1961).

The terminal velocity of a particle is evaluated by the following expression:

$$u_{p,term}=\sqrt{4gd_p(\rho_p-\rho_g)/3C_D\rho_g} \tag{11b}$$

where the drag coefficient C_D is calculated using the correlation proposed by Morsi and Alexander (1972).

The boundary conditions for the numerical solution of equations (7), (8) and (10) at the interface of Zones 1 and 2 are specified as follows:

$$\dot{M}_{slurry,2}, w_{l,2}, u_{p,2}, w_{g,2,}\ T_{p,2}, T_g = T_{g,2\to 1},\ c_{p,g} = c_{p,g,2\to 1},\ \dot{M}_{g,2} = \dot{M}_{g,2\to 1} \text{ and } PSD \qquad (12)$$

3.2.3 Zone 3 (Annular Plug-Flow Zone) and Zone 4 (Hot Core Zone)

In Figure 4 between z = 0.14 to 0.59, the near-wall temperature profile is approximately 40ºC lower than the centreline values and both profiles progressively decrease from z = 0.14 to 0.59. This region is spilt into two zones: Zone 3 is an annular section with both phases present and Zone 4 is a central core of hot gas only. In the near-wall region, the droplets/particles fall in a spiral manner and continue to dry, and this consumes a considerable amount of enthalpy from the gas flow. There is a core flow of hot gas with no solid phase present and the fall in temperature is due to enthalpy transfer into the near-wall region due to mixing and the large thermal gradient between the two regions. The temperatures cross over at z = 0.14, the near-wall temperature is higher due to very hot gas leaving Zone 5(a) close to the wall into Zone 3. The centreline temperature is that of the core gas flow into Zone 4 from the conical core section Zone 6(a), and this is cooler than the near-wall value due to ingress of cold air into Zone 7 from the base of the tower.

Zone 3 ($0.88 \le r \le 1$ and $0.14 \le z \le 0.59$) is an annular counter-current plug-flow zone representing the downward flow of all the droplets/particles and a portion of the upflow of the gas. The CFD predictions of the solids concentration profiles across the radial section at five levels in this section of the tower are depicted in Figure S2 in the supplementary material. The CFD predictions reveal that there is a high concentration of particles near the wall at all levels and almost there are no particles in the central core as depicted in the inset plot in Figure S2.

Zone 4 ($0 \le r \le 0.88$ and $0.14 \le z \le 0.59$) is a semi-plug-flow zone and is simply the upward plug-flow of the remaining portion of the gas flow. Figure 7(a) is a plot of radial temperature profiles of the gas phase along the dimensionless tower height ($0.14 \le z \le 0.59$) obtained from the CFD analysis. The radial temperature profiles of the gas phase show a lower temperature in the annular region of the tower due to exchange of enthalpy with the drying droplets/particles and heat loss. The temperature in the core region of the tower decreases as the gas flows up due to mixing of gas between the core and the annular regions as well as thermal diffusion.

Figure 7(b) is a plot of radial profiles of the gas phase dimensionless mass flow (normalised by dividing with inlet gas flow) at different dimensionless heights. The mass flow profile has a minimum at the centre of the tower throughout the height. It increases away from the centre and reaches a maximum value at a certain location (around the r = 0.88 position) and then falls. The

mass flow profile at $z = 0.56$ is quite different to those at the lower positions. There is a downward flow of the gas near the wall due entrainment of gas into the spray caused by the high momentum exerted by the downward moving droplets/particles that result in reversal of the gas flow in this region. Otherwise the profiles appear to be symmetrical around the axis of the tower. The mass flow of the gas in the annular region of the tower appears to reduce with height. The absence of particles, the falling temperatures and mass flow with height in the core region of the tower are the evidence for modelling this region as a separate zone.

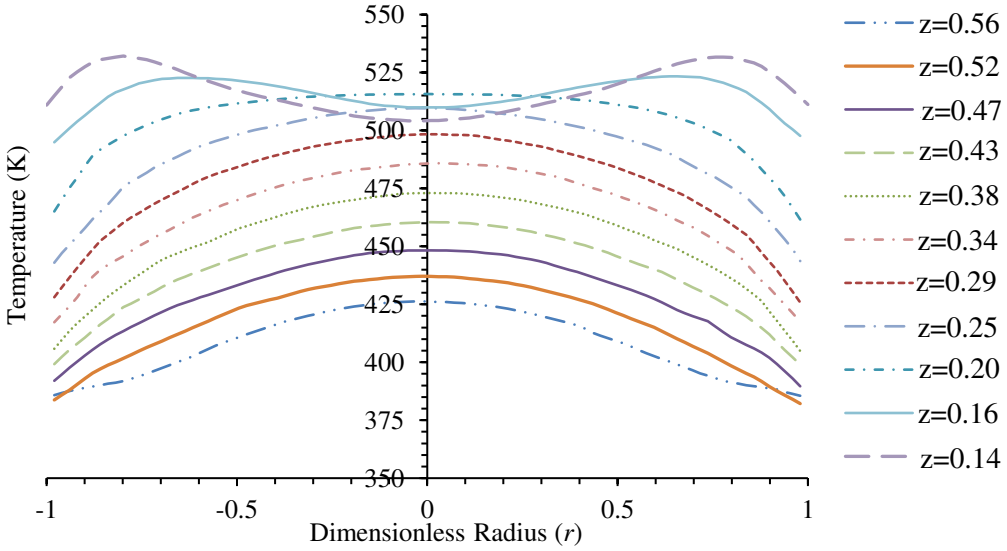

(a)

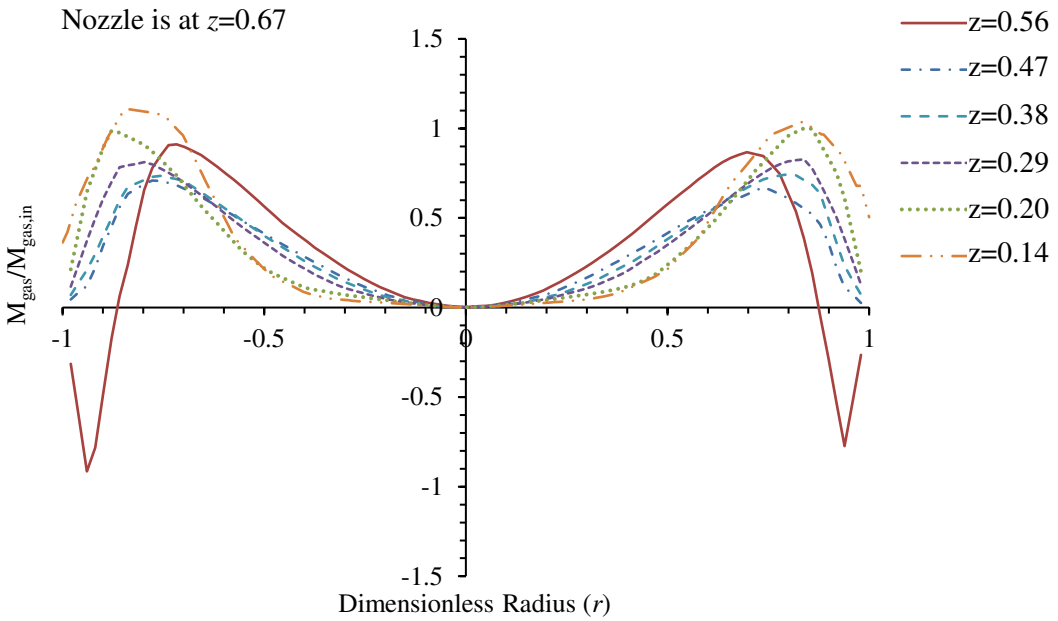

(b)

Figure 7: CFD predicted gas profiles across the radius of the tower in Zones 3 and 4 (a) gas temperature and (b) gas mass flow.

To accommodate the mixing of the gas and the heat transfer between the two parallel zones as well as the heat loss from the annular zone, the temperature profiles are represented by their respective cup mixed temperatures ($T_b(z)$). These have been evaluated from the CFD predictions by the following expression (Janna, 2000):

$$T_b(z) = \int_0^R r\bar{u}_{axial} T_g(r)\,\mathrm{d}\,r \Big/ \int_0^R r\bar{u}_{axial}\,\mathrm{d}\,r \tag{13}$$

A plot of cup mixed temperature in the core, annular and for the entire cross section of the tower at various heights in the vertical region $0.14 \le z \le 0.59$ is given in supplementary material. The solid lines represent the respective excellent curve fits to the individual data points - R^2 values greater than 0.99. The cup mixed temperature of the annular region is lower than that of the core region for a given height, and that for the entire cross-section are only slightly less than those in the core (see for details Figure S3).

The gas temperatures within Zones 3 and 4 are pre-specified along the height by the following expressions:

$$T_3 = 341.09 \times z^{-0.218} \tag{14}$$

$$T_4 = 563.23 - 282.35 \times z \tag{15}$$

The temperatures of the droplets/particles in Zone 3 are obtained in a similar manner to Zone 2 using equation (10) and the other parameters from the equations in the Appendix, but with gas temperature specified by equation (14). The velocities of the various cut sizes are specified from the residence times obtained from the CFD simulation and depicted in Figure S4 in supplementary document, which are used to estimate the best fit curve (R^2=1) of residence times of particles versus particle size in the annular region of the tower.

The boundary conditions specifications at the interface of Zones 2 and 3 for the numerical solution of the equivalent equation (10) in Zone 3 are:

$$\dot{M}_{p,2\to3}, T_{p,2\to3}, u_{p,2\to3}, w_{l,2\to3} \text{ and } \; PSD \tag{16}$$

3.2.4 Zones 5, 6 and 7 (the conical section of the tower)

The centreline temperature profile in the conical section is lower than the near-wall profile in Figure 4, which is opposite to those in the above cylindrical section. The qualitative depictions

of the CFD predictions of the gas flows and the falling droplets/particles in this section are illustrated in Figure 8 (a). These flows are split into three zones: from z = 0.031 to 0.14, Zone 5 - close to the near-wall, and Zone 6 – the core, and finally, from z = 0 to 0.031, Zone 7 – the lower conical part down to the exit. The several jets of hot gas create a severe swirl in the upper part of Zone 5. The swirl migrates downwards and the intensity lessens due to gas being entrained into the central core (Zone 6). This zone does not contain any droplets/particles and the gas flow is upwards. In Zone 7, there is a flow reversal of the gas entering from Zone 5 and also cold air is entrained through the bottom exit. The total gas flow out of Zone 7 is upwards into Zone 6, whilst the droplets/particles remain close to the wall and then exit the tower. These phenomena in Zones 5, 6 and 7 appear to be equivalent to those prevailing in a cyclone – both phases initially fall and the heavy phase (particles) remains close to wall and the lighter swirling phase (gas) migrates centrally and then the flow reverses upwards.

In order to capture the flow phenomena depicted in Figure 8 (a), the Zones 5 and 6 are each divided into five equal parts of depth 0.0218 (a) to (e) in Figure 8 (b). Each part of Zone 5 is a co-current semi-plug-flow representation (Figure 1 (f)) with the gas phase being the CSTR and the solid phase is in plug-flow, whereas each part of Zone 6 is a CSTR with only the upward flow of gas considered. The vertical interfaces between the adjacent parts of Zones 5 and 6 allow for the exchange of both enthalpy and gas flow, which are obtained from the CFD predictions. The last zone 7 is a counter-current semi-plug-flow (Figure 1 (c)) with the solid phase in plug-flow and the gas phase as a CSTR. Entrained cold air enters at z = 0 and the falling particles and a flow of gas from Zone 5 (e) enters at z = 0.031.

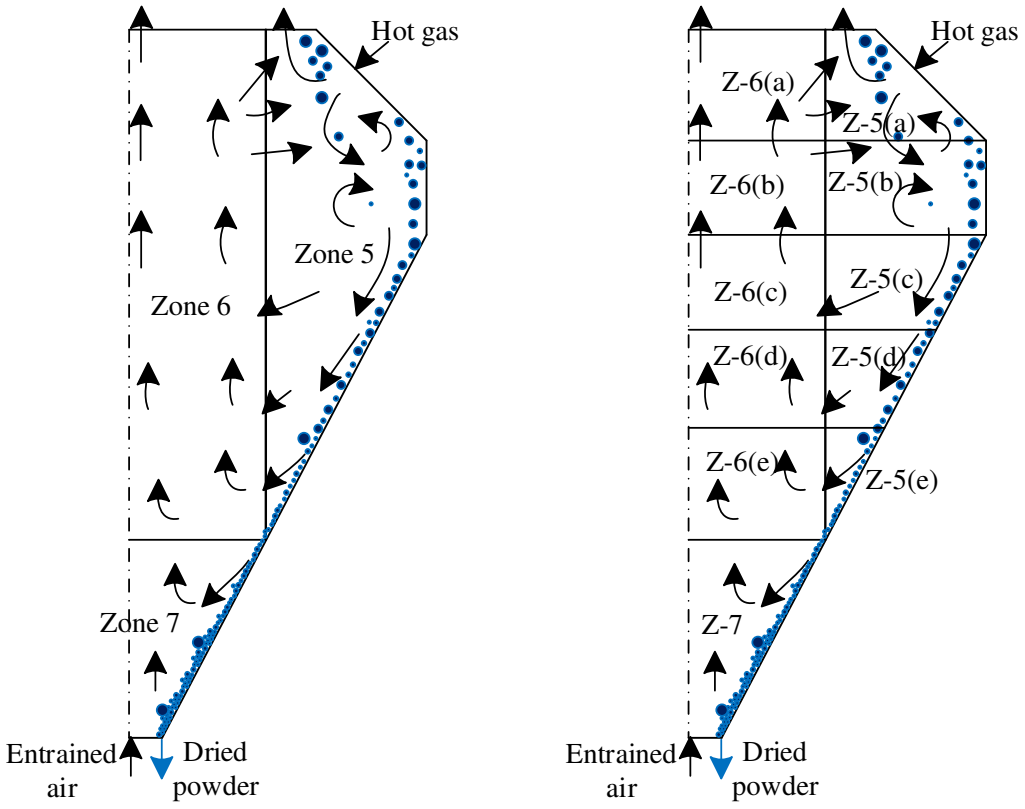

Figure 8: (a) Schematic representation of gas and droplets/particles flow patterns in zones 5, 6 and 7 of the conical section and (b) the five sub-sections of zones 5 and 6.

The enthalpy balance for the CSTR part of the semi-plug-flow representation of Zone 5(a) is equivalent to equation (4) plus the inflow of the hot gas, the flow of gas upwards into Zone 3 and any mass and enthalpy entering from or leaving to Zone 6(a). The gas temperature $T_{g,5(a)}$ within Zone 5(a) is the value leaving and entering into Zone 5(b). The following equation represents the enthalpy balance:

$$\underbrace{T_{hg,5}\dot{M}_{hg,5}c_{p,hg,5}}_{\text{Enthalpy of hot gas entering the Zone}} + \underbrace{\sum_{j=1}^{J}\left\{T_{p,j}M_{p,j}n_j\left[\left(1-w_{l,j}\right)c_p + w_{l,j}c_{p,l}\right]\right\}_{3\to 5(a)}}_{\text{Total enthalpy of droplets/particles entering the Zone}} \pm \underbrace{\dot{M}_{g,v}c_{p,g,v}T_{g,v}}_{\text{Enthalpy crossing the vertical interface of the Zone}}$$

$$= \underbrace{\left(\dot{M}_{g,5(a)\to 3} + \dot{M}_{g,5(a)\to 5(b)}\right)c_{p,g,5(a)}T_{g,5(a)}}_{\text{Enthalpy of gas leaving the Zone}} + \underbrace{\sum_{j=1}^{J}\left\{T_{p,j}M_{p,j}n_j\left[\left(1-w_{l,j}\right)c_p + w_{l,j,}c_{p,l}\right]\right\}_{5(a)\to 5(b)}}_{\text{Total enthapy of particles leaving the Zone}} \qquad (17)$$

$$+ \underbrace{2\pi\left(\tilde{r}_i HU\right)_{5(a)}\left(T_{g,5(a)} - T_{amb}\right)}_{\text{Heat loss from Zone}}$$

The temperature profiles of the various cuts of the PSD throughout Zone 5(a) are obtained in a similar way to those in Zones 2 and 3 by the numerical solution of the equivalent equation (10), but with the gas temperature equal to $T_{g,5(a)}$. The velocities of the various cut sizes are specified

from values obtained by interpolation of the residence times obtained from the CFD simulation from the exit from Zone 3 to the end of Zone 7 (see Figure S5 in the supplementary material). The gas and droplet/particle temperatures for Zones 5(b) to (e) are obtained in a similar manner to those for Zone 5(a), but the equivalent equation to (17) will not have the terms for the inlet hot gas nor the upward flow of gas.

The gas temperatures in each subsection of Zone 6 are the outlet values entering the next upper section. A heat balance equivalent to equation (17), but without any terms relating to the particles or to heat loss. The outlet temperature of the gas $T_{g,7\to6(e)}$ from Zone 7 is obtained from a slightly modified equation (17) – the inlet gas is now the entrained cold air. The temperature profiles of the droplets/particles are obtained from the solution of equation (10) with the gas temperature equal to $T_{g,7\to6(e)}$.

The numerical solution of this multi-zonal model of the tower will require an iterative procedure due to the connectivity of the zones and the next section details the solution methodology.

3.2.5 Solution Methodology

All variables required for the calculations to be carried out for the various configurations of the zones are either specified from the inlet conditions in Table 1 or obtained from the CFD predictions. These range from mass flows and temperatures of the particles and gas, the cuts of the PSD and the moisture contents of the particles and gas stream. The flow of droplets/particles of sizes < 100 μm and a portion of 200 μm entering Zone 1 from Zone 2 are fixed at the values obtained from the CFD simulation. The solution algorithm contains one outer loop and two internal loops in order to accommodate the boundary value nature of the overall system and is illustrated in the supplementary Figure S6.

The calculation starts from the tower top with estimated values of both the exhaust gas temperature ($T_{g,1\to0}$) and mass flow ($M_{g,1\to0}$), which are obtained from overall mass and energy balances assuming zero moisture in the dried powder. These initial estimates are used to calculate the gas temperature $T_{g,2\to1}$ at the interface of Zones 1 and 2 using equation (4). This requires the temperatures and moisture contents of the entrained droplets/particles and the mass flow of the gas ($M_{g,2\to1}$) at the interface of Zones 1 and 2. For the first iteration, the entrained droplets/particles have the same temperature and moisture content as the initial slurry (feed) droplets, while the gas mass flow ($M_{g,2\to1}$) is the estimated ($M_{g,1\to0}$) minus the moisture contained in the entrained droplets. This gas temperature ($T_{g,2\to1}$) along with other variables in

equation (12) are used to initiate the numerical integration by finite difference approximations of equations (7) to (11) downwards through Zone 2 to the interfaces Zones 3 and 4. A forward difference method is used for equation (10) whilst a backward difference method is used for equation (7). The calculated gas temperature at the interface of Zone 2 with Zones 3 and 4 ($T_{g,3-4\rightarrow 2}$) is compared to the cup mixed gas temperature of Zones 3 and 4 (obtained from CFD and plotted in Figure S3 in the supplementary material). If the difference is within the tolerance limit of 0.5 K, the solution moves on to Zones 3 and 4, otherwise, the temperature at the interface of Zones 1 and 2 ($T_{g,2\rightarrow 1}$) is adjusted and the calculation is repeated until the required tolerance level is achieved.

The temperatures of the gas in Zones 3 and 4 are evaluated from cup mixed relationships with height by equations (14) and (15) respectively. A numerical solution of equation (10) provides the temperature profiles of the droplets/particles using the information specified in equation (16). The values of the variables emanating from Zones 3 and 4 provide for the calculations in Zones 5, 6 and 7 – the conical section of the tower.

These calculations are part of the second inner loop of the algorithm. The adjacent sub-sections of Zones 5 and 6 are interconnected due to gas flow and enthalpy crossing the common vertical interface in either direction. All of these values are obtained from the CFD simulations. The sequence of calculations starts with an estimated value of $T_{g,6(a)\rightarrow 4}$ for the evaluation of the temperature of the gas $T_{g,5(a)\rightarrow 5(b)}$ within Zone 5(a) from equation (17). Again the temperature profiles of the various cuts of the PSD are obtained from equation (10) with the gas temperature equal to $T_{g,5(a)\rightarrow 5(b)}$. These calculations are repeated down the sub-sections to provide the temperature values of the gas $T_{g,5(e)\rightarrow 7}$ and the droplets/particles $T_{p,j,5(e)\rightarrow 7}$. From Zone 7 a new value of the gas temperature $T_{g,7\rightarrow 6(e)}$ is obtained from a modified equation (17) and the temperatures and moisture contents of the droplets/particles in a similar manner to that for the subsections of Zone 5. The temperature values of the rising gas in the sub-sections 6(e) to 6(a) $T_{g,6(e)\rightarrow 6(d)}$ to $T_{g,6(a)\rightarrow 4}$ are again obtained from an enthalpy balance – a modified form of equation (17). This evaluated value of the gas temperature now leaving Zone 6(a) $T_{g,6(a)\rightarrow 4}$ is initially compared to the original estimated temperature. If a preset tolerance of 0.1 K is acceptable, convergence has been achieved, otherwise the iteration is repeated with the latest value until convergence is attained.

To complete the overall iterative solution, it is necessary to re-evaluate the value of the gas mass flow ($M_{g,1\rightarrow 0}$) at the exit of Zone 1 by the following mass balance:

$$\dot{M}_{g,1\rightarrow 0} = \dot{M}_{hg} + \dot{M}_{cg} + \dot{M}_{evap,T} \tag{18}$$

where

$$\dot{M}_{evap,T} = \dot{M}_{slurry} - \dot{M}_{solids} \tag{19}$$

and

$$\dot{M}_{solids} = \sum_{j=1}^{J} M_{p,j,7\rightarrow 0} \times n_{p,j} + \sum_{j=1}^{J} M_{p,j,1\rightarrow 0} \times n_{p,j} \tag{20}$$

The solution is converged when the difference in the values of $\dot{M}_{g,1\rightarrow 0}$ between two successive iterations is less than a specified tolerance of 0.5%. The solution methodology is implemented in the computer software package MATLAB (2015) and the time required to achieve a converged solution was less than 1 minute on a desktop PC. The time to compute the three dimensional simulation took 1 week on a quad core processor (2.8 GHz).

A sensitivity study was carried out on the overall mass and energy balances to assess the influence of the number of increments used in the numerical integrations in the various zones represented by plug-flow and semi-plug-flow simulations. At a step height (Δz) of 1.5×10^{-3}, no appreciable change in the overall mass and energy balances was observed upon further lowering of the value of Δz. The overall mass balance error was 0.01% and the overall energy balance error was 6.8%. Higher error in the energy balance is primarily due to the use of gas temperature profiles obtained from CFD within Zones 3 and 4.

4. Results and Discussion

The calculated gas temperature profiles through the zones are plotted against dimensionless height in Figure 9 and the centreline and near-wall profiles obtained from CFD are illustrated in Figure 4. The stepwise nature of the temperatures throughout Zones 5 (a) to (e), Zone 6(a) to (e) and the constant value in Zone 7 are a consequence of the gas phase being represented by a CSTR relationship in the semi-plug-models.

The sequence of sub-zones in Zone 5 are equivalent annular regions close to the contour of the conical section through which the particles fall along with the spinning gas. The highest temperature occurs in Zone 5 (a) and this is where the hot gas enters the tower. Then the values fall quite dramatically as the gas flows downwards towards the bottom due to further drying of the falling particles throughout each sub zone. The profiles for the subzones of Zone 6 are lower

than those in Zone 5, because this is the central core region with gas flowing upwards with no particles present. The constant temperature in Zone 7 is relatively high, but this represents the value entering Zone 6(e) – the core part of the conical region. The gas temperature profiles through Zones 2, 3 and 4 are to be expected. The profiles are specified from CFD predictions in Zones 3 and 4, and in Zone 2 there is considerable drying of the atomized slurry emanating from the inlet nozzle. The lowest temperature in the simulation is in Zone 1, which lies above the nozzle to top of the tower. The value is a constant because Zone 1 is represented by a co-current CSTR model. The gas and entrained dried fine particles exit at this common temperature.

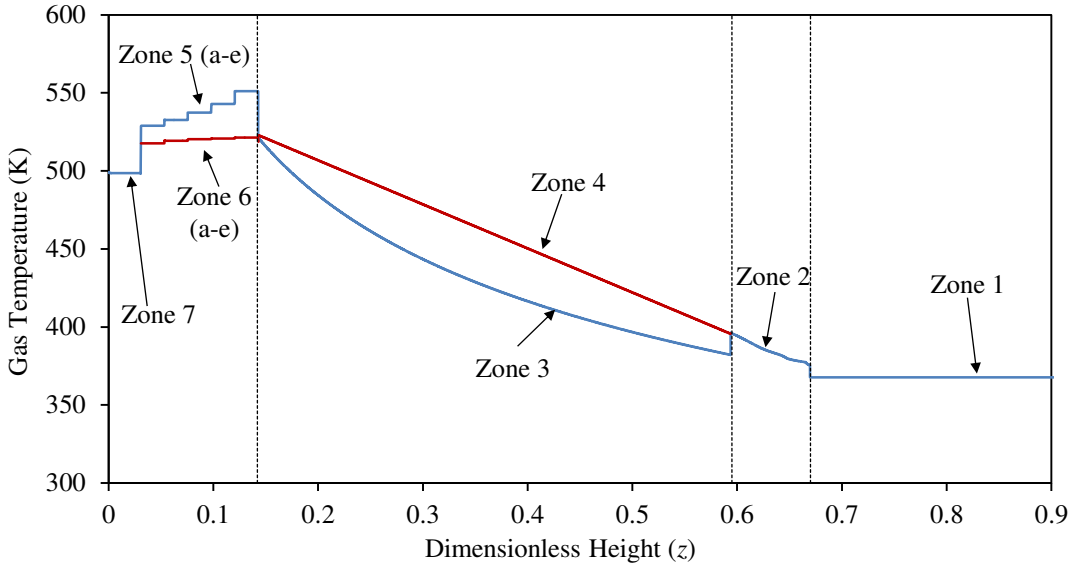

Figure 9: Calculated gas temperature profiles through the various zones.

Figure 10(a) is a plot of temperature of particles that exit from the bottom of the tower obtained from CFD (Ali *et al.*, 2017), multi-zonal and plug-flow (Ali *et al.*, 2014) models for the same input conditions. As can be seen, the predicted general trends are similar. The smaller particles exit at a higher uniform temperature and the larger particles exit at a fairly lower uniform temperature. However, the temperature of smaller particles and the particle size range over which the temperature deceases rapidly depend on the modelling approach. The plug-flow model predicts the highest temperature for the smaller particles (up to 500 µm). A sharp decrease in the exit particle temperature occurs for sizes in the range of 600 to 1000 µm. The exit temperature of particles greater than 1000 µm is fairly constant and for sizes greater than 1400 µm, it coincides with the results of CFD and zonal models. In the multi-zonal model, the exit temperatures of particles up to 700 µm are slightly smaller compared to the plug-flow model, since a well-mixed assumption is used to model the bottom region of the tower and has a lower gas temperature compared to the gas inlet temperature. A sharp decrease in the exit particle temperature occurs for sizes in the range of 800 to 1200 µm. The larger particles (>1200 µm)

exit at a constant temperature. The exit temperature of particle sizes in the range of 800 to 1200 µm is larger compared to the plug-flow model because in the zonal model, residence times obtained from CFD are used, which are larger compared to the plug-flow predicted residence times (Figure 10(c)). The CFD model predicts the lowest exit particle temperature for sizes in the range of 200 to 700 µm compared with that calculated using the multi-zonal and the plug-flow model for similar size ranges. This is because in the CFD model, the particles come in contact with cold entrained air in the conical bottom region of the tower before they exit and the smallest particles are dryer and have a higher specific surface area per unit volume therefore they quickly lose temperature upon contact with cold air.

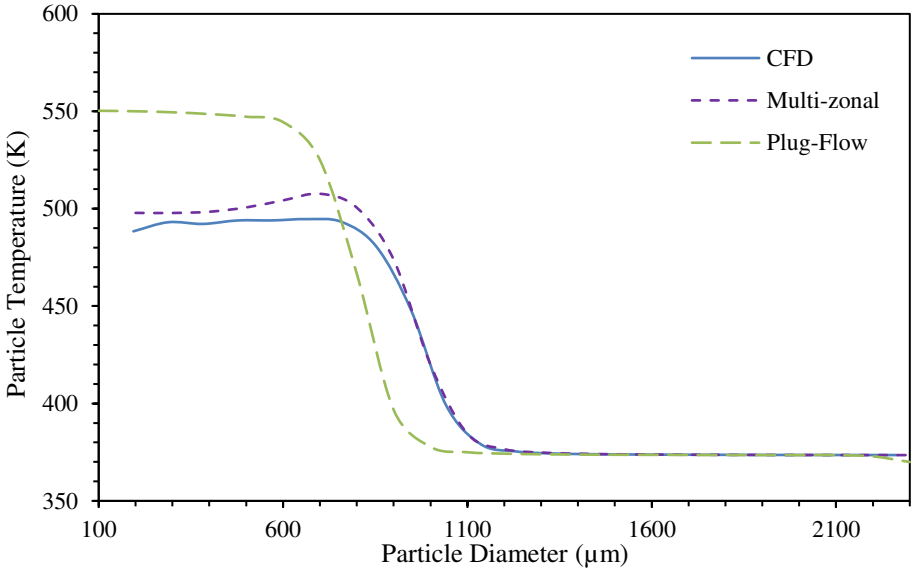

(a)

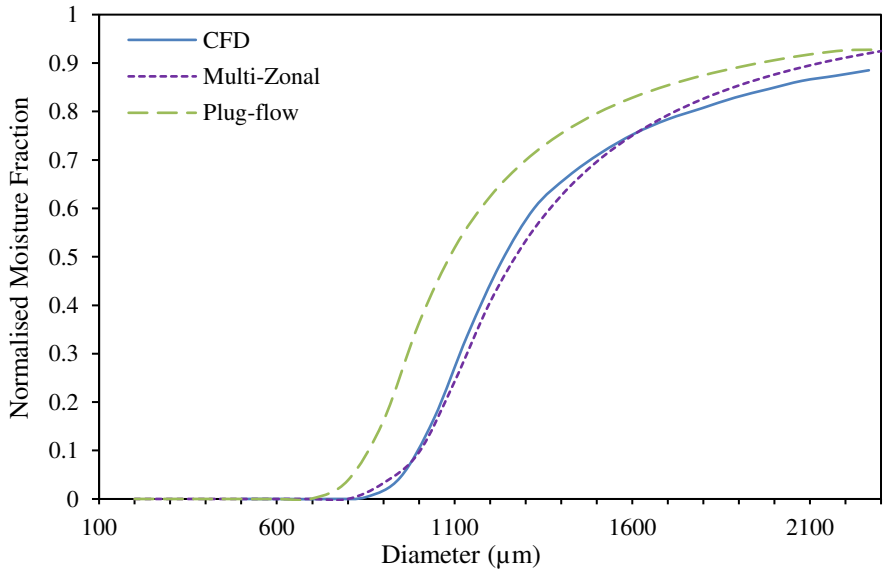

(b)

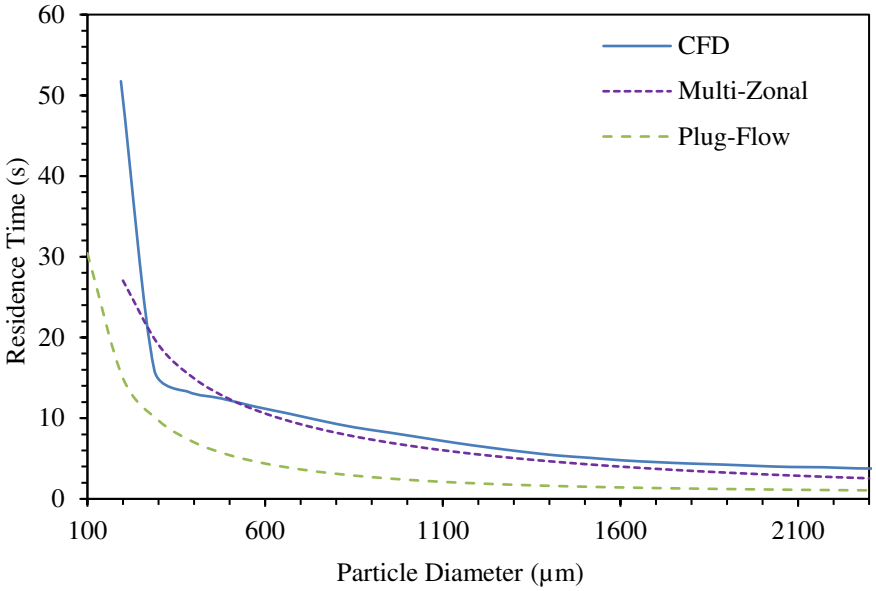

(c)

Figure 10: Calculated particle (a) exit temperatures and (b) normalized moisture content at the exit and (c) residence times obtained from the three different modelling methodologies.

Figure 10(b) is a plot of normalised moisture fraction of particles exiting from the tower bottom obtained from the three models. Again the predicted trends are qualitatively very similar, i.e. the smaller particles exit with zero moisture content while the moisture content increases with increasing particles size and follow an S-shape curve. The exit moisture profile of particles predicted by the multi-zonal model agrees extremely well to that of the CFD simulation. In the plug-flow model, particles greater than 700 µm exit at a higher moisture content compared to both the multi-zonal and CFD predictions primarily due to lower residence times caused by the plug-flow nature of the model (see Figure 10(c)).

Figure 10(c) is a plot of the predicted residence times of the exiting particles as a function of their size. Qualitatively, the trend in the residence time distribution is very similar for all three modelling approaches. As expected, the smaller particles take longer to exit from the bottom of the tower while the larger ones exit more quickly. The plug-flow model predicts the shortest residence time for all particles sizes compared to the other two models. Because in the plug-flow model, the particle-wall interaction as well as recirculation of the particles and entrainment are not considered. The CFD model predicts a very long residence time for the smallest particle size (200 µm) as they are caught up in the recirculation regions close to the injection location. In the multi-zonal model, the residence time of droplets/particles in Zone 2 (spray zone) is calculated by solving the equation of motion and the residence times in Zones 3, 5 and 7 are obtained from the CFD simulation. The residence times of larger particles (≥ 500 µm) in the multi-zonal models

are very similar to that obtained from the CFD simulation, because such particles do not get caught up in the recirculation zones near the nozzle due to greater momentum.

The weighted average particle outlet temperature and moisture content, and heat loss from the tower obtained from the multi-zonal, CFD and plug-flow simulations are listed in Table 2. The particle average moisture content is very similar in both the multi-zonal and the CFD predictions, and are slightly lower than plug-flow value. There is reasonable agreement between the particle temperatures predicted by the multi-zonal approach with multiple zones in the dryer bottom cone region and the CFD, but the plug-flow value is higher by around 26 K. Considering a single zone in the bottom cone region of the dryer also results in significantly higher exiting particle temperature. The heat loss predictions by all three simulations are very similar. Overall, the multi-zonal description of the tower provides predictions that are in a closer agreement with those from the 3-dimensional CFD approach compared to the 1-dimensional plug-flow simulation.

Table 2: Average results from the multi-zonal, CFD and plug-flow models.

Parameter	Multi-Zonal	Multi-Zonal (single bottom cone zone)	CFD	Plug-Flow
Particle weighted average normalised moisture content, %	0.15	0.15	0.16	0.2
Particle weighted average temperature, K	464.7	485.7	456.2	482.2
Heat loss, W/m^2	40.9	40.9	39.4	40.1

5. Concluding Remarks

A multi-zonal modelling methodology is proposed to provide relatively quick simulations (seconds) on desktop computers of industrial spray towers in order to avoid the extremely long (weeks) and tedious CFD simulations on high performance computers for quick decision making on changing process parameters for automatic process control. The zonal model will comprise combinations of six zonal representations: plug-flow, semi-plug-flow and well-mixed CSTR zones in either co- or counter-current flow. This approach is successfully applied to model the spray drying process of a detergent slurry in an industrial counter-current spray drying tower. The location and type of these zones are based upon the detailed analysis of predictions from our previous 3-dimensional CFD simulation (Ali *et al.*, 2017) of radial and axial distributions of the gas and the particle temperatures, the moisture contents as well as the particle trajectories and

residence times. The tower is divided into three distinct regions and 7 zones overall: the region above the spray nozzle to the top is represented by one co-current CSTR, the region below the nozzle down to the conical part has two counter-current plug-flow zones coupled to one plug-flow zone with only gas flow, and the conical section where the hot gas enters has three zones comprising one co-current plug-flow, one plug-flow with only gas flow and finally one counter-current semi-plug-flow. Interestingly the tower itself is operated counter-currently, but the multi-zonal representation consists of both co- and counter-current zones. These interconnected zones and mathematical descriptions with the slurry and hot gas entering at different locations result in a boundary value problem, which necessitates an iterative solution technique. An algorithm consisting of one outer iteration loop and two internal loops and a logic flow diagram is presented.

The data required to run the multi-zonal simulation are the original input specifications for the CFD investigation (Table 1) and values extracted from the CFD predictions including the gas temperature for the calculation of cup mixed temperature profiles in zones 3 and 4 (using equations (14) and (15)). The residence times of particles in zone 3 and in the bottom conical zone are also taken from CFD for the calculation of particle velocities in these zones. For modelling the bottom cone zones, the gas mass and enthalpy fluxes across the zones are also obtained from CFD. The PSD (100 μm to 2300 μm) of the atomised slurry is represented by 23 equal sized cuts. The fines of 100 μm and a portion of 200 μm sizes are entrained by the upward flowing gas and leave at the top of the tower with the gas. The rest of the particles leave at the bottom of the tower. The results obtained from this multi-zonal modelling methodology are compared with the predictions obtained from both the CFD and the plug-flow model (Ali *et al.*, 2014) investigations.

The gas temperature profiles in the tower follow very similar trends to those observed in the CFD predictions. The particle exit temperatures, moisture contents and the particle residence times over the full PSD range are extremely close to the CFD values unlike the plug-flow simulated results. The average weighted particle temperatures are within 8 K and the percentage moisture contents are within 0.01 for the multi-zonal and CFD calculations. For the plug-flow results the temperature is around 26 K higher and the percentage moisture content is higher by 0.04, which are caused by the shorter residence times in the simulation.

The run times for the multi-zonal algorithm and the plug-flow simulation are around one minute on a desktop PC, whilst the CFD simulation takes around one week on a quad core processor (2.8 GHz). These excellent results justify the time and effort in developing the multi-zonal model of this counter-current tower and the further analysis of the CFD predictions has revealed very

illuminating aspects of the very complex physical phenomena occurring. Cyclonic gas and particle flows exists in the bottom section of the tower. The multi-zonal modelling methodology can be used for online process control applications as it rapidly predicts reliably dried powder characteristics and is very fast.

Acknowledgements

This work was partially sponsored by Procter and Gamble Technical Centres, Newcastle-upon-Tyne, UK. The authors thank Mr Zayeed Alam for his support and co-ordination and Dr Hossein Ahmadian and Prof. Andrew Bayly for useful discussions.

Nomenclature

α	convective film coefficient (W/m^{2}K)
C_D	drag coefficient
c_p	specific heat (J/kgK)
D_{AW}	diffusivity of vapours in air (m^2/s)
d_p	droplet/particle diameter (m)
d_m	size constant (m)
g	acceleration due to gravity (m^2/s)
H	height (m)
$\dot{h}$	enthalpy flow (J/kgs)
h_{fg}	latent heat of vapourisation (J/kg)
M	mass (kg)
$\dot{M}$	mass flow (kg/s)
n	number flow of particles (1/s)
PSD	particle size distribution
p	Pressure
$\dot{Q}$	heat flux (W/m^2)
r	normalised radial location
r_o	radius of nozzle (m)
r_c	radius of air core (m)
r_p	droplet/particle radius (m)
T	temperature (K)
t	time (s)

U	overall heat transfer coefficient (W/m^{2}K)
u	velocity (m/s)
u_s	distribution parameter
u_{axial}	axial velocity (m/s)
w_l	moisture fraction (wt/wt)
Y_d	cumulative frequency oversize
z	normalised tower height

Greek letters

ρ	density (kg/m^3)
λ	thermal conductivity (W/mK)
μ	viscosity (kg/ms)
φ	specific humidity
θ	spray cone injection angle

Subscripts

amb	ambient
drop/p	of the droplet/particle
g	of the gas
i	of the inside
l	of the liquid
sat	at saturation
slurry	of the slurry
solids	of the solids
vap	of the vapour

References

Ali, M. (2014). Numerical modelling of a counter-current spray drying tower. PhD Thesis, University of Leeds, UK.

Ali, M., Mahmud, T., Heggs, P. J., Ghadiri, M., Djurdjevic, D., Ahmadian, H., Juan, L. M., Amador, C. and Bayly, A. (2014) A one-dimensional plug-flow model of a counter-current spray drying tower. *Chem. Eng. Res. Des.*, vol. 92, pp. 826-841.

Ali, M., Mahmud, T., Heggs, P. J., Ghadiri, M., Bayly, A., Ahmadian, H. and Juan, L. M. (2017). CFD modelling of a pilot-scale counter-current spray drying tower for the manufacture of detergent powder. *Drying Technology*, vol. 35 (3), pp. 281-299.

Ade-John, A. O. and Jeffreys, G. V. (1978). Flow visualization and residence time studies in a spray drier. *Trans IChemE*, vol. 56, pp. 36-42.

Anandharamakrishnan, C., Gimbun, J., Stapley, A. G. F. and Rilley, C. D. (2010). A study of particle histories during spray drying using computational fluid dynamic simulations. *Drying Technology*, vol. 28, pp. 566-576.

Crank, J., 1975. The Mathematics of Diffusion, second ed. Clarendon Press, Oxford.

Crowe, C. T. (1983). Droplet-gas interaction in counter-current spray dryers. *Drying Technology*, vol. 1, pp. 35-56.

Francia, V., Martin, L., Bayly, A. E. and Simmons, M. J. H. (2015). The role of wall deposition and re-entrainment in swirl spray dryers. *AIChE J.*, vol. 61, pp. 1804-1821.

Gauvin, W. H., Katta, S. and Knelman, F. H. (1975). Drop trajectory predictions and their importance in the design of spray dryers. *Int. J. Multiphas. Flow*, vol. 1, pp. 793-816.

Griffith, J. D., Bayly, A. E. and Johns, M L. (2008). Magnetic resonance studies of detergent drop drying. *Chem. Eng. Sci.*, vol. 63, pp. 3449-3456.

Harvie, D. J. E., Langrish, T. A. G. and Fletcher, D. F. (2002). A computational fluid dynamics study of a tall-form spray dryer. *Trans IChemE*, vol. 80, pp. 163-175.

Hecht, J. P. and King, C. J. (2000). Spray Drying: Influence of Developing Drop Morphology on Drying Rates and Retention of Volatile Substances. 2: Modeling. *Ind. Eng. Chem.*, vol. 39, pp. 1766-1774.

Hecht, J. P. (2012). Personal Communication, P&G Technical Centres, UK.

Huang, L., Passos, M. L., Kumar, K. and Mujumdar, A. S. (2004). A three-dimensional simulation of a spray dryer with a rotary atomizer. Drying 2004 – Proceedings of the 14th international drying symposium (IDS 2004), vol. A, pp. 319-325.

Huang, L. and Mujumdar, A. S. (2006). Numerical study of two-stage horizontal spray dryer using computational fluid dynamics, *Drying Technology*, vol. 24, pp. 727-733.

Huang, L. X., Kumar, K. and Mujumdar, A. S. (2006). A comparative study of a spray dryer with rotary disc atomizer and pressure nozzle using computational fluid dynamic simulations. *Chem. Engg. Proc.*, vol. 45, pp. 461-470.

Janna, W. S. (2000). *Engineering heat transfer*. Florida: CRC Press.

Katta, S. and Gauvin, W. H. (1975). Some fundamental aspects of spray drying. *AIChE J.*, vol. 21, pp. 143-152.

Keey, R. B. and Pham, Q. T. (1976). Behaviour of spray dryers with nozzle atomisers. *The Chemical Engineer*, 311, pp. 516-521.

Kieviet, F. G. (1997) Modelling Quality in spray drying. Eindhoven. *University of Technology*, PhD Thesis.

Kieviet, F. G. and Kerkhof, P. J. A. M. (1997). Air flow, temperature and humidity patterns in a co-current spray dryer: modelling and measurements. *Drying Technology*, vol. 15, pp. 1763-1773.

Langrish, T. A. G. and Zbicinski, I. (1994). The effects of air inlet geometry and spray cone angle on the wall deposition rate in spray dryers. *Trans IChemE*, vol. 72 (A), pp. 420-430.

Livesley, D. M., Oakley, D. E., Gillespie, R. F., Ranpuria, C. K., Taylor, T., Wood, W. and Yeoman, M. L. (1992). *Development and validation of a computational model for spray-gas mixing in spray dryers*. Drying '92, Ed. Mujumdar, A. S., pp. 407-416, New York: Hemisphere Publishing Corp.

MATLAB v. 8.6.0. The MathWorks Inc., 2015.

Mezhericher, M., Levy, A. and Borde, I. (2008). Droplet-droplet interactions in spray drying by using 2D computational fluid dynamics. *Drying Technology*, vol. 26, pp. 265- 282.

Mezhericher, M., Levy, A. and Borde, I. (2010). Spray drying modelling based on advanced droplet drying kinetics. *Chem. Eng. Proc.*, vol. 49, pp. 1205–1213.

Mezhericher, M., Levy, A. and Borde, I. (2012). Probabilistic hard-sphere model of binary particle–particle interactions in multiphase flow of spray dryers. *International Journal of Multiphase Flow*, vol. 43, pp. 22–38.

Montazer-Rahmati, M. M. and Ghafele-Bashi, S. H. (2007). Improved Differential Modeling and Performance Simulation of Slurry Spray Dryers as Verified by Industrial Data. *Drying Technology*, vol. 25 (9), pp. 1451-1462.

Morsi, S. A. and Alexander, A. J. (1972). An investigation of particle trajectories in two-phase flow systems. *J. Fluid Mech.*, vol. 55 (2), pp. 193-208.

Nelson, P. A. and Stevens, W. F. (1961). Size distribution of droplets from centrifugal spray nozzles. *AIChE J.*, vol. 7(1), pp. 80-86.

Oakley, D. E. and Bahu, R. E. (1993). Computational modelling of spray dryers. *European symposium on Computer Aided Process Engineering-2*, pp. 493-498.

Parti, M. and Palancz, B. (1974). Mathematical model for spray drying. *Chem. Eng. Sci.*, vol. 29, pp. 355-362.

Pinto, M., Kemp, I, Bermingham, S., Hartwig, T. and Bisten, A. (2014). Development of an axisymmetric population balance model for spray drying and validation against experimental data and CFD simulations. *Chem. Eng. Res. Des.*, vol. 92, pp. 619-634.

Ranz, W. E. and Marshall, W. R. (1952). Evaporation from drops. *Chem. Eng. Prog.*, vol. 48, pp. 141–146; 173-180.

Rosin, P. and Rammler, E. (1933). The Laws Governing the Fineness of Powdered Coal. *Journal of the Institute of Fuel*, vol. **7**, pp. 29-36.

Southwell, D. B., Langrish, T. A. G. and Fletcher, D. F. (1999). Process intensification in spray dryers by turbulence enhancement. *Trans IChemE*, vol. 77, Part A, pp. 189-205.

Straatsma, J., Houwelingen, G. V., Steenbergen, A. E. and Jong, P. D. (1999). Spray drying of food products: 1. Simulation model. *J. Food Engg.*, vol. 42, pp. 67-72.

Topar, J. (1980). Mathematical model of spray drying reckoning with droplet size distribution. *Drying'80: Proceedings of the second international drying symposium*, vol. 2, pp. 405-409.

Wawrzyniak, P., Podyma, M., Zbicinski, I. Bartczak, Z., Polanczyk, A. and Rabaeva, J. (2012). Model of heat and mass transfer in an industrial counter-current spray drying tower. *Drying Technology*, vol. (30), pp. 1274-1282.

Zbicinski, I. (1995). Development and experimental verification of momentum, heat and mass transfer model in spray drying. *The Chem. Eng. J.*, vol. 58, pp. 123-133.

Zbicinski, I. and Zietara, R. (2004). CFD model of counter-current spray drying process. *Proceedings of the 14th International Drying Symposium*, 2004, Sao Paulo, 22-25 August, vol. A, pp. 169-176.

APPENDIX A. Single droplet drying model

Drying model assumptions

The following assumptions are made in the development of the single droplet/particle drying model in this discourse:

1. There are no temperature gradients within the droplet/particle. Since the droplets/particles are very small (ranging from 50 μm to 2300 μm), the variation of temperature within the droplet can be neglected.
2. Internal circulation inside the slurry droplet is neglected. The droplet sizes are relatively small and the presence of solid particles inside the droplet hampers internal circulation of the liquid.
3. The droplets and the resulting particles remain spherical throughout the tower. This assumption holds true for small droplets. The simulation of droplets/particles with non-spherical symmetry involves excessive complexity, which may not be worth the additional effort at this stage.
4. The density and specific heat of the slurry, and the diffusivity of vapours into the air remains constant.
5. Each resulting droplet is assumed to contain a single centrally located saturated vapour bubble, which will grow as the droplet gets heated up and the boiling temperature is reached. Initial bubble size is assumed to be small enough that it does not affect the size of the droplet/particles in the first two stages of drying. Hence it is neglected in these stages. The

bubble is allowed to grow in the puffing stage. The initial size of the bubble is defined by the user. Actual particles may contain more than one bubble. The size of the bubble is kept constant once the size of the particle becomes equal to the initial droplet size. Hence no change in the particle size occurs once the particle size becomes equal to the size of the initial droplet. Although particle may undergo several episodes of inflation and deflation and possible rupture, which is not considered in the model due to the complexities involved in predicting the extent to which the particle inflates/deflates.

Governing Equations

The moisture content in the droplet is calculated using the equation proposed by Hecht and King (2000):

$$\tilde{u}_p \frac{\mathrm{d}\, w_l}{\mathrm{d}\, z} = \frac{(1-w_l)^2}{M_{solid}} \frac{\mathrm{d}M_p}{\mathrm{d}t} \tag{A.1}$$

The change in droplet radius due to evaporation of liquid in the first stage of drying is given by:

$$\tilde{u}_p \frac{\mathrm{d}r_p}{\mathrm{d}z} = \frac{-\left(\frac{\mathrm{d}M_p}{\mathrm{d}t}\right)}{4\pi\rho_l {r_p}^2} \tag{A.2}$$

The new droplet diameter is given by:

$$d_{p,new} = d_p - 2\,\Delta r_p \tag{A.3}$$

In the first stage of drying, the evaporation of moisture from the surface of the droplet depends upon the vapour concentration at the surface and the relative humidity of air. Thus the rate of evaporation from the droplet is proportional to the difference between the actual moisture concentration at the surface (C_s) and the moisture content at the surface which is in equilibrium with the moisture in the bulk (C_∞). The initial slurry droplet drying rate based on surface drying is given by:

$$\frac{\mathrm{d}M_p}{\mathrm{d}t} = 4\pi {r_p}^2 K k_c (C_s - C_\infty) \tag{A.4}$$

In the above equation, K is the partition coefficient, which is the ratio of concentration of water vapour in the gas phase to the concentration of water in the liquid phase inside the droplet.

$$K = \frac{C_v}{C_s} \cong \frac{\varphi \rho_{gas}}{w_{l,initial} \rho_{slurry}} \tag{A.5}$$

k_c in equation (A.4) the mass transfer coefficient, is given by:

$$k_c = \frac{\mathrm{Sh} \times D_{AW}}{d_p} \tag{A.6}$$

and the Sherwood number (Sh) predicted from the Ranz and Marshall (1952) correlation as follows:

$$\mathrm{Sh} = 2.0 + 0.6 \times \mathrm{Re}^{0.5}\, \mathrm{Sc}^{1/3} \tag{A.7}$$

The surface moisture concentration (C_s) is obtained by solving the diffusion equation in planar coordinates system for diffusion in a semi-infinite slab. This predicts the surface concentration well as long as it is limited to the near-surface positions and not deep into the droplet, as compared to the droplet radius. The equation for diffusive mass transport is given by:

$$\underbrace{\frac{\partial C}{\partial t}}_{\substack{\text{Net change in} \\ \text{concentration}}} = \underbrace{D_{WS} \frac{\partial^2 C}{\partial x^2}}_{\substack{\text{Change in concentration} \\ \text{by diffusion}}} \tag{A.8}$$

In equation (A.8), the diffusivity (internal diffusion of moisture, D_{WS}) is assumed to be constant. The value of D_{WS} has been determined experimentally.

The initial condition for equation (A.8) is:

$$\text{for } t < 0 \text{ and } 0 \le x \le \infty : C = C_i \tag{A.9}$$

The boundary conditions for $t \geq 0$ are:

at x = 0: $$-D_{WS}\frac{\partial C}{\partial x} = k_c(C_\infty - C_s) \quad \text{(A.10)}$$

at $x \to \infty$: $$C = C_i \quad \text{(A.11)}$$

where x is zero at the surface.

The analytical solution of the diffusion equation (A.8) along with the initial and boundary conditions (A.9), (A.10) and (A.11) is given by Crank (1975) and the surface concentration (at x = 0) is given by the following expression:

$$\frac{(C_s - C_i)}{(C_\infty - C_i)} = 1 - \exp\left(\left(\frac{K\,k_c}{D_{WS}}\right)^2 D_{WS}\,t\right) \times \text{erfc}\left(\left(\frac{K\,k_c}{D_{WS}}\right)\sqrt{D_{WS}\,t}\right) \quad \text{(A.12)}$$

where erfc is the complementary error function and C_i is the initial concentration of the moisture in the droplet. This equation (A.12) is simplified by introducing the following dimensional parameter:

$$B = K\,k_c\sqrt{\frac{t}{D_{WS}}} \quad \text{(A.13)}$$

Equation (A.12) now becomes:

$$\frac{(C_s - C_i)}{(C_\infty - C_i)} = 1 - \exp\left(B^2\right) \times \text{erfc}(B) \quad \text{(A.14)}$$

Typically, the moisture from the droplet surface is removed faster than it can diffuse from the interior of the droplet and this causes the surface to dry. The time for the surface to achieve 90% of the equilibrium moisture content is given by:

$$\exp\left(B^2\right) \times \text{erfc}(B) = 0.1 \quad \text{(A.15)}$$

The solution of equation (A.15) results in:

$$B = 5.5 \quad \text{(A.16)}$$

From equations (A.16) and (A.13), the time needed for surface of a particle/droplet to reach a dryness value equivalent to 90% of the equilibrium concentration, t_{sd} is given by:

$$t_{sd} = D_{WS}\left(\frac{5.5}{K\,k_c}\right)^2 \tag{A.17}$$

Once the surface is dry, the drying rate becomes dependent on internal diffusion of moisture. An algebraic equation for this step was obtained by fitting results from a full numerical model for droplet drying model developed by Hecht and King (2000). The drying rate for this stage is given by:

$$\frac{\mathrm{d}M_p}{\mathrm{d}t} = r_p \times 10^6 \times \exp\left[-\mathrm{A}\left(\frac{t - t_{sd}}{r_p \times 10^6}\right)^{\mathrm{B}} - \mathrm{C}\right] \tag{A.18}$$

where A, B and C are constants for the exponential curve fit with values of 18.9, 0.2 and 17.7, respectively.

Puffing starts when the particle temperature exceeds the boiling point of the slurry. The methodology assumes an initial saturated vapour bubble of diameter 1 μm inside the particle and this is provided as an input. The particle diameter is increased accordingly. During the puffing stage, the drying process is controlled by external heat transfer from the air to the particle. As the particle dries, the boiling temperature of the slurry increases. The drying rate is obtained by a simple energy balance on a single particle, with the boiling temperature of the slurry represented as a function of moisture content:

$$\frac{\mathrm{d}M_l}{\mathrm{d}t} = -\frac{\alpha_p\, 4\pi\, r_p^{\,2}\,(T_g - T_p)}{h_{fg} - \left(w_s\, c_{p,s} + w_l\, c_{p,l}\right) w_s\, \dfrac{\mathrm{d}T_{boil}}{\mathrm{d}w_l}} \tag{A.19}$$

The relationship between the boiling point of the detergent slurry and moisture content was determined experimentally by P&G and is given by:

$$T_{boil} = \exp\left(\frac{276.25}{23.68 + 100\, w_l} - 6.6\right) + 373.15 \tag{A.20}$$

During puffing, it is assumed that the evaporated water is trapped inside the particle in the form of a saturated vapour bubble. The bubble inside the particle expands as the particle temperature rises. This causes inflation of the particle. The pressure inside the bubble is calculated using the equation given by Hecht and King (2000):

$$p_{bubble} = p + \frac{2\sigma}{r_{bubble}} \tag{A.21}$$

The new bubble radius is calculated using the ideal gas law:

$$r_{bubble,new} = \left(\frac{3N_{vap}R_gT_p}{4\pi\, p_{bubble}} \right)^{1/3} \tag{A.22}$$

where N_{vap} is number of moles of moisture vapour inside the bubble. The inflated particle radius is calculated using the following equation:

$$r_{p,new} = \sqrt[3]{r_{bubble,new}^3 + r_p^3} \tag{A.23}$$

The particle is not allowed to inflate above the initial droplet size, since the model does not capture the multiple inflation/deflation periods and possible rupture of the particle.

The droplet/particle velocity for each particle size is calculated from the equation of motion:

$$\underbrace{M_p \tilde{u}_p \frac{\mathrm{d}u_p}{\mathrm{d}z}}_{\text{Change in droplet/particle momentum}} = \underbrace{M_p g}_{\text{droplet/particle weight}} + \underbrace{\vec{F}_a}_{\text{Bouyancy force}} + \underbrace{\vec{F}_d}_{\text{Drag force}} \tag{A.24}$$

The buoyancy force ($\vec{F}_a$) is given by:

$$\vec{F}_a = -M_p g \left(\frac{\rho_g}{\rho_p} \right) \vec{i} \tag{A.25}$$

The drag force ($\vec{F}_d$) in equation (A.24) is given by:

$$\vec{F}_d = -\frac{1}{2}\rho_g \pi r_p^2 C_D \left|u_p - u_g\right|\left(u_p - u_g\right) \tag{A.26}$$

The Reynolds number based on the relative velocity is given by:

$$\mathrm{Re} = \frac{\rho_g d_p \left|u_p - u_g\right|}{\mu_g} \tag{A.27}$$

The drag coefficient correlation for spherical bodies proposed by Morsi and Alexander (1972) is used for droplets and particles and is given by:

$$C_D = a_1 + \frac{a_2}{\mathrm{Re}} + \frac{a_3}{\mathrm{Re}^2} \tag{A.28}$$

where a_1, a_2 and a_3 are constants for several ranges of particle Reynolds number and given below:

a_1	a_2	a_3	Applicable Re range
0	24	0	$0 < \mathrm{Re} \leq 0.1$
3.69	22.73	0.0903	$0.1 < \mathrm{Re} \leq 1$
1.222	29.167	-3.889	$1.0 < \mathrm{Re} \leq 10$
0.6167	46.5	-116.667	$10 < \mathrm{Re} \leq 100$
0.3644	98.33	-2778	$100 < \mathrm{Re} \leq 1000$
0.357	148.62	-4.75×10^4	$1000 < \mathrm{Re} \leq 5000$
0.46	-490.546	57.87×10^4	$5000 < \mathrm{Re} \leq 10000$
0.5191	-1662.5	5.4167×10^6	$\mathrm{Re} > 10000$